Spike-Timing Patterns Conform to Gamma Distribution with Regional and Cell Type-Specific Characteristics

Meng Li[1], Kun Xie[1], Hui Kuang[1], Jun Liu[1], Deheng Wang[1], Grace E. Fox[1], Wei Wei[3], Xiaojian Li[1], Yuhui Li[1], Fang Zhao[1], Liang Chen[4], Zhifeng Shi[4], He Cui[2], Ying Mao[4] & Joe Z. Tsien[1]*

[1]Brain and Behavior Discovery Institute and Department of Neurology, Augusta University, Augusta, GA 30912, USA

[2]Institute of Neuroscience, Chinese Academy of Sciences, Shanghai 200031, China

[3] The Brain Decoding Center, BanNa Biomedical Research Institute, Yunnan Academy of Science and Technology, Yunnan 666106, China

[4]Neuropathology, Huashan Hospital, Fudan University, Shanghai 200040, China

*Correspondence author

E-mail: jtsien@augusta.edu (JZT)

Abstract

Spike-timing patterns are crucial for synaptic plasticity and neural computation, yet their statistical patterns in various brain regions which cross different mammalian species have not been examined in a systematic manner. Neurons *in vivo* discharge spikes with enormous variability. This irregularity often models as a Poisson-like random process. Here, we systematically examine statistical behaviors of spike-time irregularity in 13 different cortical and subcortical regions from mouse, hamster, cat and monkey brains. We show that spike-timing patterns of interneurons and various projection neurons - including cortical excitatory principal cells, hippocampal pyramidal cells, inhibitory striatal medium spiny neurons, as well as dopaminergic neurons – all conform to the gamma distribution model. Moreover, gamma shapes of spike-timing patterns remain robust over different states - such as sleep and awake periods and under fearful events. Interestingly, there are significant regional variations of the spike-timing's regularities - that is, DA neurons, the somatosensory cortex and motor cortices showing increased regularity, whereas the V1 cortex, retrosplenial cortex, anterior cingulate cortex, striatum, amygdala, and hippocampus tend to exhibit greater irregularity. Furthermore, we observe that ketamine-induced anesthesia largely deranges the gamma-like spike-timing patterns. Such a conserved gamma distribution pattern, coupled with characteristic regional variations, may influence how spike-timing patterns exert dynamic actions on neural coding and network-level plasticity.

Author summary

Spike-timing patterns are crucial for synaptic plasticity and neural computation, yet their statistical patterns in various brain regions which cross different mammalian species have not been examined in a systematic manner. We examined statistical behaviors of spike-time irregularity in 13 different cortical and subcortical regions from mouse, hamster, cat and monkey brains. We show that spike-timing patterns of interneurons and various projection neurons all conform to the gamma distribution model. Furthermore, there are significant regional variations of the spike-timing's regularities, and ketamine-induced anesthesia largely deranges the gamma-like spike-timing patterns. Such intrinsic statistical characteristics of spiking-time distribution will likely influence not only how spike-timing patterns drive synaptic plasticity, but also how cell assemblies in various circuits perform the neural computation.

Introduction

Spike-timing patterns play important roles in synaptic plasticity and neural computation [1-6]. During cognitions and behaviors, neurons discharge their spikes *in vivo* with tremendous variability in both the "control" resting states and across trials within the same experiments in response to identical stimuli [7-9]. This variability is widely assumed to reflect noises or uncontrolled internal variables derived from synaptic, cellular and network levels [10, 11]. Intriguingly, it is known that neurons are capable of generating precisely-timed spikes in response to fluctuating currents injected at the soma [12-14]. It has been shown that in spite of "channel noise" [9], deterministic neuronal models can accurately predict stimulus responses [15].

The irregularity of inter-spike intervals has long been suggested to be a fundamental process of cortical communication [6, 16-20], and it was often modeled as a Poisson-like random process. Intriguingly, a growing number of observations have shown that the neuronal spike pattern in many cortical areas seems to be inconsistent with the Poisson process, indicating that the Poisson process can either under- or overestimate the variabilities of the neuronal spike patterns [21-28]. Despite the importance in regulating synaptic plasticity and neural coding, spike-time patterns across a wide range of brain regions and animal species have not been examined or compared in a systematic manner. It remains to be demonstrated whether statistical features of spike patterns in various brain regions would conform to a particular set of mathematical properties and models (e.g., log-normal distribution, gamma distribution, and/or Poisson model). Systematic characterizations of spike-time patterns in a brain-wide manner would be valuable towards the better understanding of how neural coding is achieved and modified by synaptic plasticity upon learning.

In the present study, we set out to apply a series of statistical analyses on large-scale *in vivo* datasets of neuronal spike activity collected from 13 cortical and subcortical regions from four different animal species - namely, mice, hamsters, cats and monkeys. Our analyses show that the spike patterns of interneurons and various principal projection neurons - including excitatory cortical cells, CA1 pyramidal cells, inhibitory medium spiny neurons in the striatum, as well as dopaminergic (DA) neurons from the ventral tegmental area (VTA) - all follow positive-skewed, long-tailed distribution. We then conducted the goodness-of-fit analyses and demonstrate that the positive-skewed spike patterns can be statistically characterized much better by the gamma distribution model rather than the log-normal distribution model. Furthermore, we found that the overall gamma distribution shapes of the positive-skewed spike patterns remain robust against the changes of firing rates across distinct cognitive states, such as sleep, awake periods and under fearful events. However, neurons in different regions or animal species exhibit distinct tendencies in the degrees of irregularities of spike dynamics. We further show that the gamma-like spike-timing patterns could be largely deranged under “dissociative anesthesia” (incapable of associating the input of afferent stimuli, and integrating information and signals to the conscious mind is reduced or blocked), indicating there is strong relevance between the gamma-like spike-timing patterns and information processing within neural circuits.

Results

Statistical properties of neural spike-timing patterns

Neural spike activities are highly variable even in the quiet-awake resting state (upper subpanel of Figure 1A), and the distributions of the single unit's spike patterns showed that they are skewed with heavy tails (lower subpanel of Figure 1A). We set out to conduct a two-step analysis to explore the statistical properties of neural spike patterns.

Figure 1. Statistical properties of neural spike patterns

(**A**) Neuronal spikes are highly variable. The upper subpanel illustrates the spike-activity patterns of 20 neurons within a 10-sec time period recorded from the VTA region of a mouse during the awake state. The lower subpanel shows the ISI distribution of a sample VTA DA neuron.

(**B**) Illustrations of a positive- and negative-skewed distribution. The red and blue curves illustrate a positive-skewed distribution and a negative-skewed distribution, respectively. Gray dashed lines denote a symmetric distributions. Skewness (γ) and nonparametric-skew (S) are applied to examine the positive/negative-skewed properties.

(**C**) Illustrations of a gamma distribution model and a log-normal distribution model. Fitted gamma distribution and log-normal distribution of the ISI in the lower subpanel of (**A**) are plotted as red and blue curves. The goodness-of-fit analysis is conducted to compare the gamma distribution model with the log-normal distribution model for characterizing neuronal spike patterns.

Step 1: Does the neural spike pattern follow a positive-skewed or negative-skewed distribution (Figure 1B)? We characterized the distribution of inter-spike intervals (ISIs) for

neural spike patterns by using two well-defined statistics - namely, nonparametric-skew (S) and skewness (γ) (see Materials and Methods). In statistics, these two parameters are measurements of the skewness (or long-tailedness) of a random variable's distribution – that is, the distribution's tendency to lean to one side or the other of the mean (Figure 1B). A positive-skewed distribution (red curve in Figure 1B) has $S > 0$ and $\gamma > 0$, a negative-skewed distribution (blue curve in Figure 1B) has $S < 0$ and $\gamma < 0$, while a symmetric distribution (gray dotted curves in Figure 1B) has $S = 0$ and $\gamma = 0$.

Step 2: We then considered the problem of selecting the best-fitting statistical distribution model to characterize the positive-skewed distribution. As two widely-used distributions for modeling and analyzing non-negative skewed data - namely, the gamma distribution model and the log-normal distribution model – these models were considered as alternatives for comparison (see Materials and Methods). The gamma distribution and log-normal distribution have been previously applied for modeling firing patterns of neuron population [29] and spike patterns of single neurons [30, 31].

In Figure 1C, the ISI distribution shown in Figure 1A was analyzed here as an illustrative example. It is evident that the gamma-distribution model provided more accurate-fitting results than the log-normal distribution model. It should be noted that the parameters of both gamma and log-normal distributions in all datasets were directly estimated from the raw ISIs of neuronal spike activities by using the maximum likelihood estimates (MLE) method, which guaranteed that the analyses of ISI distributions were independent of the bin sizes used for the illustrations of ISI histograms.

We then conducted goodness-of-fit analyses to quantitatively discriminate between the gamma distribution model and log-normal distribution model. The ratio of maximized likelihoods (RML), which is a statistical test used for comparing the goodness-

of-fit of two models [32-34], was employed for discriminating the gamma distribution model and the log-normal distribution model. The natural logarithm of RML, denoted as D, was calculated as the measurement of the goodness-of-fit (see Materials and Methods). That is, the gamma distribution model precedes the log-normal distribution model if $D > 0$; otherwise, choose the log-normal distribution as the preferred model. The larger the absolute value of D, the more accurate-fitting the result of the chosen model over the other model.

In the following sections, we conducted this two-step analyses on *in vivo* datasets of neuronal spike activity recorded from a wide range of cortical and subcortical areas under one or multiple brain states or experimental conditions in mice, hamsters, cats and monkeys.

Spike-timing patterns of principal cells conformed to gamma distribution across different brain regions of mice under the quiet-awake state

We used 128-channel tetrode arrays to record neurons from four cortical and subcortical regions - namely, anterior cingulate cortex (ACC), retrosplenial cortex (RSC), hippocampal CA1, and the basolateral amygdala (BLA) - in freely-behaving mice. The qualities of recorded neurons were quantitatively measured by “Isolation Distance” [35], neurons whose “Isolation Distance” >15 were selected for the present analysis. To facilitate direct comparison, we focused on putative principal cells after being separated from putative fast-spiking interneurons (see Materials and Methods). In addition, to minimize the potential state-dependent influence on neuronal variability, we used the spike datasets collected from the quiet-awake state as animals rested in their home-cage environments.

We calculated nonparametric-skew (S) and skewness (γ) on four putative principal cell datasets recorded from four brain regions - namely, ACC (neuron number n=197), RSC (n=321), hippocampal CA1 (n=511) and BLA (n=451). Our results showed that all the principal cells in these four brain regions exhibited similar positive-skewed distributions (Figures 2A-D). Skewness (γ) had a range of 1-10 (ACC = 3.82±0.11, RSC = 2.98±0.07, CA1 = 3.92±0.08, and BLA = 3.55±0.09, data were shown as mean ± SEM). Nonparametric-skew (S) were all in a range of 0.2-0.5 (ACC = 0.346±0.003, RSC = 0.335±0.001, CA1 = 0.335±0.002 and BLA = 0.358±0.003, data were shown as mean ± SEM). These results clearly demonstrated that the neuronal spike patterns in these four brain regions of mice followed positive-skewed, long-tailed distributions.

Figure 2. Putative principal cells in mice's cortical and subcortical regions discharge positive-skewed, heavy-tailed spike patterns.

(**A**) ACC, (**B**) RSC, (**C**) CA1, and (**D**) BLA. The left subpanels of (**A**-**D**) show the histograms of skewness γ in the corresponding regions, where the gray vertical lines denote the symmetric distributions (γ=0), positive-skewed distributions have $\gamma > 0$, while negative-skewed distributions have $\gamma < 0$. The middle subpanels of (**A**-**D**) show the histograms of nonparametric-skew S in the corresponding regions, the symmetric distributions have $S = 0$, $S > 0$ for positive-skewed distributions and $S < 0$ for negative-skewed distributions. The right subpanels of (**A**-**D**) show their relationships with the neurons' mean firing rates, where the colors of each dot represent the mean firing rates of corresponding neurons.

We then fitted the spike patterns of each principal cell in four brain regions when animals were in the quiet-awake state, the parameters of gamma and log-normal

distributions were estimated. To avoid the under-sampled error due to few data points, units with <250 ISIs were excluded in the present analysis. The left subpanels of Figures 3A-D showed fitted gamma and log-normal distributions of example principal cells for these four regions. D (the natural logarithm of RML) was calculated for the fitted gamma and log-normal distributions for each of the principal cells in the four brain regions. As shown in the right subpanels of Figures 3A-D, $D > 0$ was observed for all putative principal cells in the four regions, indicating that the gamma distribution outperformed on fitting neuronal spike ISIs over the log-normal distribution. Furthermore, the mean firing rates and D were highly linearly correlated in all four regions (the correlation coefficients were: 0.80 of ACC, 0.89 of RSC, 0.83 of CA1 and 0.70 of BLA).

Figure 3. Spike-timing patterns of principal cells conformed to gamma distribution across mice cortical and subcortical regions under the quiet-awake state.

(**A**) ACC, (**B**) RSC, (**C**) CA1, and (**D**) BLA. The left subpanels of (**A**-**D**) show the spike-timing patterns of sample neurons recorded from the corresponding brain regions, their fitted gamma distributions (red curves) and log-normal distributions (blue curves). The right subpanels of (**A**-**D**) are the distributions of D (the natural logarithm of RML) vs. mean firing rates of principal cells under the quiet-awake state. The lines in these plots illustrate the linear regression between D and mean firing rates of principal cells.

Spike-timing patterns of principal cells conformed to gamma distribution across different cortical and subcortical regions of mice during the animals' sleep

Since firing patterns could vary significantly in different brain states, we asked whether the gamma distribution model provided a modest description of neuronal spike

activities over different brain activity states. As such, we compared the gamma distribution and the log-normal distribution in modeling neuronal activities of principal cells recorded from the same four mice's brain regions during the animals' sleep. As shown in Figure 4, the gamma distribution model outperformed the log-normal distribution model for fitting the putative principal cells during the animals' sleep ($D > 0$ for all four brain regions). Again, the firing rates of principal cells in these four regions were also linearly correlated with D under the sleep state (the correlation coefficients between firing rates and D were: 0.93 of ACC, 0.71 of RSC, 0.86 of CA1, and 0.62 of BLA).

Figure 4. Spike-timing patterns of principal cells conformed to gamma distribution across different mice cortical and subcortical regions during the animals' sleep.

The distributions of D vs. mean firing rates of principal cells recorded from different cortical and subcortical regions during the animals' sleep. The lines in these plots illustrate the linear regression between D and mean firing rates of principal cells.

All these analyses supported the notion that the positive-skewed distribution of neuronal spike patterns can be statistically described by the gamma distribution model in different cortical and subcortical regions of mice under distinct brain states.

Preserved shape parameter *k* across brain states

Since the positive-skewed distribution is the intrinsic characteristic of neuronal spike pattern, we further examined whether there existed any invariant feature about this positive-skewed distribution across distinct brain states. Two parameters of the gamma distribution model, shape parameter k and scale parameter θ, were measured under two distinct brain states (the quiet-awake vs. sleep). In the gamma distribution model, the

shape parameter k describes the overall envelope of an ISI distribution, while the scale parameter θ is related to the mean firing rate within the uncertain state (the reciprocal of the scale parameter, $r = 1/\theta$, is known as the rate parameter). The shape parameter k provides useful measurements for spike dynamics under different cognitive states, with a higher k indicating more regular spiking discharge patterns and a lower k indicating more irregular spike activities.

Analyses were performed on four additional datasets consisting of putative principal cells recorded from four brain regions under both the quiet-awake state and the animals' sleep (34 cells from ACC, 102 cells from RSC, 43 cells from CA1, and 182 cells from BLA). The results showed that the two parameters of the gamma distribution model were correlated between awake and sleep states in all four regions (Figure 5, correlation coefficient R between k_{awake} and k_{sleep}: ACC, R=0.89; RSC, R=0.91; CA1, R=0.94; BLA, R=0.77. Correlation coefficient R between θ_{awake} and θ_{sleep}: ACC, R=0.81; RSC, R=0.71; CA1, R=0.79; BLA, R=0.48. Ps <0.0001, *t*-test).

Figure 5. Preserved shape parameter *k* across brain states.

Distributions of shape parameter k of principal cells in four brain regions during awake and sleep states are shown in the left subpanels of (**A-D**), while distributions of scale parameter θ in these two states are shown in the right subpanels. Red lines denote the linear regressions of corresponding parameters; red numbers at the upper-left corner of each subpanel denote the correlation coefficients.

We further fitted these two parameters with linear functions for visually displaying the changing trends by the slope of fitted linear dependencies (shown as the red lines and red numbers in Figure 5). We observed that the transformations of the scale parameter

θ (related to neuron's mean firing rate) between awake and sleep states were varied among these brain regions. Specifically, the mean firing rates of the principal cells in ACC remained unchanged between the two states (in the right subpanel of Figure 5A, the slopes of fitted linear dependencies was 1.003). The principal cells in RSC exhibited increased mean firing rates in the sleep state (in the right subpanel of Figure 5B, the slopes of fitted linear dependencies was 0.835). On the contrary, as shown in the right subpanels of Figures 5C and D, the slopes of fitted linear dependences of CA1 and BLA regions were 1.138 and 1.512, respectively, indicating that the mean firing rates of the principal cells in these two regions decreased in sleep states compared to awake states.

Comparing to the diverse transformations of θ, our analyses showed that the shape parameter k of the principal cells in all these four brain regions were not only highly correlated, but also remained tightly preserved between the two states (the left subpanels of Figures 5A-D, as denoted by the slopes of fitted linear dependences of k: ACC, 1.056; RSC, 1.045; CA1, 1.010 and BLA, 1.027). Given the fact that the shape parameter k is the parameter for characterizing the overall shape of ISI distribution, our results provided strong evidence for the notion that the overall shapes of positive-skewed distributions of neuronal firing patterns were preserved across distinct brain states (sleep vs. awake), which is independent of the changes in firing rates under different cognitive states.

By far, we have verified that the spike-timing patterns conformed to gamma distribution under the quiet-awake state and sleep. One may argue that the spike-timing patterns during these brain states could be represented or dominated by "noise." Therefore, to exclude such a possibility - other than by using spiking data from animals during the quiet-awake state and sleep - we further analyzed the data recorded from behaving animals. Two datasets were recorded from ACC and RSC regions during the

fearful-event experiment (three fearful episodic events were included: earthquakes, footshocks, and free-fall drops, see Materials and Methods). Three distinct brain states (the quiet-awake state, sleep and during the fearful-event experiment) were recorded for each neuron in these two datasets. A total of 95 and 120 principal cells were recorded from ACC (three mice) and RSC (four mice), respectively. As shown in Figure 6, the goodness-of-fit analysis confirmed that the spike-timing patterns followed the gamma distribution under these three brain states ($D > 0$). Furthermore, the firing rates and D were highly linearly correlated in all three brain states (left sub-panels of Figures 6A and B) with D increased with higher firing rates (the correlation coefficients between firing rates and D were: 0.94 of ACC and 0.71 of RSC for the quiet-awake state, 0.93 of ACC and 0.71 of RSC during sleep, and 0.91 of ACC and 0.84 of RSC during fearful-event experiment). Surprisingly, compared with the quiet-awake state and sleep, the gamma distribution model provided more accurate-fitting results from behaving animals (as shown by the gradients of the fitted linear relationships between firing rates and D, left sub-panels of Figures 6A and B). We also examined the robustness of the shape parameter k by calculating the correlations between these three distinct brain states, revealing that the shape parameter k was preserved not only between the quiet-awake state and sleep, but also preserved in behaving animals (right sub-panels of Figures 6A and B, the correlation coefficients were: ACC, 0.83 between the quiet-awake state and sleep, 0.75 between sleep and behaving state, and 0.71 between the quiet-awake state and behaving state; RSC, 0.96 between the quiet-awake state and sleep, 0.95 between sleep and behaving state, and 0.94 between the quiet-awake state and behaving state). Thus, our analysis demonstrated that the spike-timing patterns conformed to gamma distribution with preserved shape parameter k under both resting states (the quiet-awake state and sleep) and behaving state.

Figure 6. Preserved shape parameter *k* across resting states and behaving states.

The distributions of D vs. mean firing rates of principal cells recorded from ACC and RSC regions during two resting states (the quiet-awake state and sleep) and behaving state are shown in the left sub-panels of (**A** and **B**). The lines in the left sub-panels of (**A** and **B**) are the linear regressions between D and mean firing rates. 3-D distributions of k during three states are shown in the right sub-panels of (**A** and **B**).

Spike-timing patterns of striatal medium spiny projection neurons conformed to gamma distribution

The above analyses have shown that the neuronal spike patterns of the principal excitatory cells across different cortical and subcortical regions followed a gamma distribution. Next, we investigated whether the gamma-like spike patterns reflect a general property that would remain true for GABAergic projection neurons. Thus, we employed 128-channel recording techniques and monitored activity patterns from the dorsal striatum of freely-behaving mice in the quiet-awake state. We conducted the same statistical analysis on a dataset of 294 medium spiny projection neurons (see Materials and Methods). Being the principal projection neurons of the striatum, medium spiny projection neuron is a special type of GABAergic inhibitory cells distinct from many other types of local interneurons [36, 37].

Figure 7A showed the fitted gamma and log-normal distributions of a sample medium spiny neuron; it was evident that the gamma distribution model produced a better result for the peak of the ISI distribution. As shown in Figure 7B, skewness $\gamma = 3.77 \pm 0.10$ and nonparametric-skew $S = 0.357 \pm 0.003$ (data were shown as mean ± SEM). These

results show that the neuronal spike patterns of medium spiny projection neurons also exhibited positive-skewed, long-tailed distributions. Furthermore, the gamma distribution model achieved superior performance on fitting neuronal spike patterns of medium spiny projection neurons over the log-normal distribution model ($D > 0$ for all medium spiny projection neurons, Figure 7C).

Figure 7. Spike-timing patterns of striatum medium spiny projection neurons conformed to gamma distribution.

(**A**) The spike-timing pattern of a medium spiny projection neurons recorded from the dorsal striatum of mice, and its fitted gamma distribution (red curve) and log-normal distribution (blue curve).

(**B**) Medium spiny projection neurons discharge positive-skewed, heavy-tailed spike patterns. The upper subpanel: the histogram of γ. The middle subpanel: the histogram of S. The lower subpanel: the distribution of γ and S, where the dots' colors represent neurons' mean firing rates.

(**C**) The distribution of D vs. mean firing rates of medium spiny projection neurons. The line in the plot denotes the linear regression between D and mean firing rates.

Spike-timing patterns of VTA dopaminergic neurons conformed to gamma distribution

To further evaluate the general utility of the gamma distribution model, we then analyzed neuromodulatory projection neurons, such as dopaminergic (DA) neurons recorded from the mouse VTA region. The DA neuron dataset was collected from freely-behaving mice during the awake period as we have previously described [27, 38]. DA

neurons, which project over long distances to various cortical and subcortical sites [39-41], are well-known to subserve a wide range of biological functions, such as motivation and reward [42-45], addiction [46, 47], fear memory and behaviors [38, 48-50].

As illustrated in Figure 8A, we found that the ISI distribution of a sample VTA DA neuron can be better characterized by the gamma distribution. Skewness ($\gamma = 2.57 \pm 0.21$, mean ± SEM) and nonparametric-skew ($S = 0.263 \pm 0.010$, mean ± SEM) demonstrated that the neuronal spike patterns of VTA DA neurons followed positive-skewed distributions with heavy tails (Figure 8B). Again, the gamma distribution model outperformed the log-normal distribution model for fitting the neuronal spike patterns of VTA DA neurons ($D > 0$ for all VTA DA neurons, as shown in Figure 8C). And the firing rates were linearly correlated with D (the correlation coefficients between firing rates and D was 0.33).

Figure 8. Spike-timing patterns of VTA DA neurons conformed to gamma distribution.

(**A**) Fitted gamma distribution and log-normal distribution of the spike-timing pattern of a DA neuron recorded from mice VTA region.

(**B**) VTA DA neurons discharge positive-skewed, heavy-tailed spike-timing patterns. The upper subpanel: the histogram of γ. The middle-subpanel: the histogram of S. The lower subpanel: the distribution of γ and S, where the dots' colors represent neurons' mean firing rates.

(**C**) The distribution of D vs. mean firing rates of VTA DA neurons. The line in the plot represents the linear regression between D and mean firing rates.

Taken together, the above analyses have shown that spike-timing patterns in these long-projection principal neurons all followed a gamma distribution, regardless of cortical/subcortical regions, brain states, and distinct cell types (cortical excitatory cells, CA1 pyramidal cells, medium spiny neurons, or DA neurons). In the following section, we conducted comparative analyses on neuronal spike datasets recorded from additional mammalian species to examine if the gamma-like spike patterns were universal properties of neuronal spike activities.

Spike-timing patterns of principal cells in the hamster prelimbic region conformed to gamma distribution

We asked whether the excitatory units in the prelimbic region (PrL) of Golden Syrian hamsters would follow the gamma-like spike patterns. As described in our previous study [51], we implanted 64-channel tetrode arrays bilaterally into the PrL region and recorded neural-activity patterns when animals were in their quiet-awake states. A total of 200 putative excitatory principal cells recorded from 13 hamsters were identified as stable and well-isolated units for the analyses.

The gamma and log-normal models of a sample PrL principal cell were shown in Figure 9A. The spike patterns of these cells exhibited clearly positive-skewed, heavy-tailed distributions (Figure 9B, $\gamma = 3.78 \pm 0.12$, $S = 0.341 \pm 0.003$, mean ± SEM). The goodness-of-fit analysis showed that all PrL excitatory principal cells can be better described by using the gamma distribution models (Figure 9C, $D > 0$ for all PrL excitatory principal cells), and D was linearly correlated with the mean firing rates (correlation coefficient is 0.79). Together, we showed that these putative principal cells in the hamster PrL cortex also followed the gamma distribution model.

Figure 9. Spike-timing patterns of principal cells in hamster PrL region conformed to gamma distribution.

(**A**) Fitted gamma distribution and log-normal distribution of a principal cell recorded from hamster PrL region.

(**B**) Principal cells in hamster PrL region discharge positive-skewed, heavy-tailed spike patterns. The upper subpanel: the histogram of γ. The middle subpanel: the histogram of S. The lower subpanel: the distribution of γ and S, where the dots' colors represent neurons' mean firing rates.

(**C**) The distribution of D vs. mean firing rates of principal cells in the hamster PrL region. The line in the plot represents the linear regression between D and mean firing rates.

Spike-timing patterns in monkey posterior parietal cortex area 5d conformed to gamma distribution

In addition to the analysis of neuronal spike patterns recorded in the brains of rodents (mouse and hamster), we further asked whether spike-time patterns in other advanced species also followed the gamma distribution. We analyzed the datasets collected from rhesus monkeys (Li and Cui, 2013). In this study, the single-neuron activities were recorded from the dorsal area 5 (area 5d) on the gyral surface adjacent to the medial bank of the intraparietal sulcus, which is closely linked to movement kinematics [52] and movement preparation [53]. Briefly, the monkeys were required to touch the fixation center at the trial beginning. Then, the first- and second-reaching goals were simultaneously displayed for 400 ms with a green square and triangle (shifted by 135° counterclockwise from the square), respectively. After a 600 ms delay, the central green dot turned off (GO signal), and the monkeys were allowed to initiate the reaching

sequence to touch the locations previously cued by the square and triangle in the correct order. Throughout the trial, the monkeys were either required to maintain eye fixation (fixation condition) at the center or allowed to move their eyes freely (free-view condition). Single-reach trials were pseudo-randomly interleaved with the double-reach trials for control. Here, we analyzed a total of 211 neurons and observed that the spike patterns of monkey area 5d neurons also exhibited obvious positive-skewed distributions (Figures 10A and B, $\gamma = 17.81 \pm 1.37$, $S = 0.219 \pm 0.007$, mean ± SEM), and can be modeled by gamma-distribution (Figure 10C, $D > 0$ for all area 5d neurons, the correlation coefficient between D and mean firing rates was 0.42).

Figure 10. Spike-timing patterns in monkey area 5d conformed to gamma distribution.

(**A**) Fitted gamma distribution and log-normal distribution of a sample neuron recorded from monkey area 5d.

(**B**) Neurons in area 5d discharge positive-skewed, heavy-tailed spike patterns. The upper subpanel: the histogram of γ. The middle-subpanel: the histogram of S. The lower subpanel: the distribution of γ and S, where the dots' colors represent neurons' mean firing rates.

(**C**) The distribution of D vs. mean firing rates of neurons in area 5d. The line in the plot denotes the linear regression between D and mean firing rates.

Spike-timing patterns in cat primary visual cortex conformed to gamma distribution

Finally, we analyzed a dataset of extracellular recordings from the primary visual cortex of anesthetized adult cats that were deposited in the public domain (Dan et al.,

2009). This dataset was originally performed for measuring the spatiotemporal receptive fields of cortical cells [54-57]. One of two different visual stimuli, either 1-D white noise [473 neurons, 1-D white noise (random bars) aligned to the preferred orientation of each cell] or 2-D stimuli (202 neurons, natural images, natural phase, and random phase), were delivered to the anesthetized cats. Thus, this dataset was not only ideal for verifying the gamma distribution model but also afforded an opportunity to examine if the gamma distribution model was robust under two different types of stimulus conditions.

Figure 11. Spike-timing patterns in cat primary visual cortex conformed to gamma distribution.

(**A** and **B**) Fitted gamma distributions and log-normal distributions of two neurons recorded from cat primary visual cortex under 1-D white noise (**A**) and 2-D stimuli (**B**).

(**C** and **D**) Neurons in cat primary visual cortex discharge positive-skewed, heavy-tailed spike patterns under both 1-D white noise (**C**) and 2-D stimuli (**D**). The upper subpanels: the histograms of γ. The middle subpanels: the histograms of S. The lower subpanels: the distributions of γ and S, where the dots' colors represent neurons' mean firing rates.

(**E** and **F**) The distributions of D vs. mean firing rates of neurons in cat primary visual cortex under 1-D white noise (**E**) and 2-D stimuli (**F**). The line in the plot denotes the linear regression between D and mean firing rates.

First, we observed that the spike patterns of the neurons in the primary visual cortex of cats all followed positive-skewed distribution under 1-D white noise (Figures 11A and C, $\gamma = 2.80 \pm 0.04$, $S = 0.421 \pm 0.004$, mean ± SEM) and 2-D stimuli (Figures 11B and D, $\gamma = 2.81 \pm 0.05$, $S = 0.392 \pm 0.006$, mean ± SEM). Furthermore, the distributions of γ

and S showed no significant differences under these two distinct types of stimuli ($p > 0.94$, *t*-test). Second, the goodness-of-fit analysis demonstrated that the gamma distribution outperformed the log-normal distribution for characterizing the spike patterns of the primary visual cortex neurons under both 1-D white noise and 2-D stimuli (Figures 11E and F, the correlation coefficients between D and mean firing rates were 0.44 for 1-D white noise and 0.41 for 2-D stimuli). These results demonstrated that spike-timing patterns in the primary visual cortex of cats also followed the gamma distribution model, and overall gamma distribution remained robust over different stimulus types.

Spike-timing patterns of interneurons conformed to gamma distribution

To further verify that the gamma-like spike-timing patterns were a universal characteristic of neuronal spike activity, we set out to examine if the neuronal spike patterns of inhibitory interneurons also followed a gamma distribution. A total of 136 interneurons recorded from four mice brain regions (36 from ACC, 31 from BLA, 32 from hippocampal CA1, and 37 from RSC) were analyzed. As shown in Figures 12A and B, the neuronal spike patterns of interneurons also exhibited positive-skewed, long-tailed distributions ($\gamma = 4.68 \pm 0.24$, $S = 0.327 \pm 0.004$, mean ± SEM). The goodness-of-fit analysis showed that the spike patterns of all these inhibitory interneurons followed the gamma distribution models (Figure 12C, $D > 0$ for all these interneurons, the correlation coefficient between D and mean firing rates was 0.75). These results strongly supported the conclusion that the addition to principal cells in different brain regions, the spike-timing patterns of inhibitory interneurons also followed the gamma distribution.

Figure 12. Spike-timing patterns of interneurons conformed to gamma distribution.

(**A**) Interneurons recorded from four brain regions (ACC, BLA, hippocampal CA1, and RSC) discharge positive-skewed, heavy-tailed spike patterns. The left subpanel: the histogram of γ. The right subpanel: the histogram of S.

(**B**) The distribution of γ and S, where the dots' colors represent neurons' mean firing rates.

(**C**) The distribution of D vs. mean firing rates. The line in the plot denotes the linear regression between D and mean firing rates.

Regularities of spike-timing patterns across different brain regions

Given the critical roles of spike-timing patterns in synaptic plasticity and neural computations, we further ask how spike dynamics vary over different brain regions. Therefore, we systematically compared the regularities of neuronal spike patterns in a wide range of brain regions and further included additional datasets we have collected from the V1 cortex, secondary auditory cortex, and somatosensory cortex of behaving mice. The total datasets consisted of a total of 3,186 neurons obtained from 13 brain regions of four species. Specifically, we analyzed datasets collected from nine mouse brain regions as follows: 84 DA neurons from the VTA, 85 excitatory principal cells from the somatosensory cortex, 615 excitatory principal cells from the RSC, 342 excitatory principal cells in the V1, 325 CA1 pyramidal cells, 41 excitatory principal cells recorded from the 2nd auditory cortex (2nd AuV), 195 excitatory principal cells from the ACC, 263 pyramidal cells in the BLA, and 221 medium spiny neurons in the STR. Moreover, we also analyzed 182 excitatory principal cells from the hamster PrL; 475 units in the cat V1

during 1-D white noise and 207 excitatory principal cells from the cat V1 area during 2-D stimuli, as well as 206 excitatory cells in the monkey brain area 5d.

We compared the regularities of neuronal spike patterns in these brain regions by examining the shape parameters k of their gamma distribution patterns. Based on its definition, k provides an effective way to measure neuronal spike patterns' regularities. A gamma distribution with $k=1$ is the mathematical equivalent to an exponential distribution, the corresponding neuronal spike pattern fits a Poisson process (shown as the gray horizontal line in Figure 13). Neuronal spike patterns with $k<1$ indicate that the neuron discharges more frequently in short and long intervals than the exponential distribution – namely, irregular spiking. When $k>1$, the peaks of ISI distributions shift away from zero, and the neuron discharges more regular spiking than the Poisson process. Gamma distribution with $k=\infty$ is the distribution of no variance, and the corresponding neuronal spike pattern is perfectly regular.

Figure 13. Spike-timing regularities across different brain regions.

The distributions of k in 13 brain regions recorded from four mammalian species (mice, hamster, cat and monkey). Each dot represents a neuron. The gray horizontal line denotes the Poisson process ($k=1$), regular spiking ($k>1$) and irregular spiking ($k<1$) are shown as a red-arrow line and blue-arrow line, respectively. Error bars represent mean ± SEM.

As shown in Figure 13, we observed that the neuronal spike patterns in most brain regions exhibited more irregular spiking than the Poisson process [k : 0.921±0.008 in RSC, 0.844±0.015 in V1, 0.825±0.010 in CA1, 0.793±0.018 in Hamster PrL, 0.719±0.040 in 2nd AuV, 0.689±0.015 in ACC, 0.632±0.013 in BLA, 0.601±0.014 in STR, 0.636±0.013 in Cat V1 (2-D), and 0.530±0.007 in Cat V1 (1-D), shown as mean ± SEM]. While neurons in the

other three brain regions discharged more regular spiking than the Poisson process (k: 1.806±0.104 by DA neurons from the mouse VTA, 1.610±0.055 in the monkey brain motor area 5d, and 1.240±0.039 in the mouse somatosensory cortex, shown as mean ± SEM), there were significant differences between three regular-spiking regions in comparison to 10 irregular-spiking regions ($p < 0.0001$, One-way ANOVA coupled with Tukey's posthoc test).

Gamma-like spike-timing patterns diminished under anesthesia

To further test the hypothesis that the gamma-like spike-timing pattern serves as an information carrier for neural computation, we predict that the gamma-like spike-timing patterns will diminish under the condition when both external and internal neural computation is artificially shut down, *i.e.,* upon anesthesia. Accordingly, we recorded neuronal spike activities from the mouse BLA, CA1, and RSC regions, in the awake state as well as under ketamine/domitor-induced anesthesia. We then examined how anesthesia affected the distributions of ISI from the same set of putative pyramidal neurons. Indeed, in all these three brain regions, the gamma-like spike-timing patterns of putative pyramidal cells deranged dramatically upon ketamine-induced anesthesia. The differences were evident from ketamine-induced rhythmic spike discharge patterns (Figures 14A-C). Furthermore, the frequencies of the rhythmic spike patterns were different in these brain regions - specifically, BLA > CA1> RSC (as shown in the right sub-panels of Figures 14A-C).

Figure 14. Gamma-like spike-timing patterns diminished under anesthesia.

(**A-C**) Spike activities of 15 example principal cells recorded during the awake state and anesthesia from BLA (**A**), CA1 (**B**), and RSC (**C**).

(**D-F**) Left subpanels: spike-timing patterns under the quiet-awake state conform to single gamma distribution. Right subpanels: spike-timing patterns during ketamine-induced anesthesia can be described by using two gamma distributions. The subplots show the similarity between the empirical cumulative probabilities and the cumulative probabilities of corresponding fitted gamma distributions. The one-sample Kolmogorov-Smirnov test is applied to verify the fitness of the gamma distribution.

We further examined the ISI distributions of pyramidal cells under the awake state and ketamine-induced anesthesia. As shown in the left sub-panels of Figures 14D-F, the spike patterns of pyramidal cells in these three regions conformed to the gamma distribution model. However, the spike patterns of these pyramidal cells during anesthesia cannot be described by a single gamma distribution (p<1E-5, one-sample Kolmogorov-Smirnov test). Nevertheless, as shown in the right sub-panels of Figure 14D-F, these patterns can be modeled by using two gamma distributions.

These pharmacological intervention experiments demonstrated that the shutting down of external and internal coding processes indeed greatly influenced neuronal spike patterns. This again was consistent with the notion that gamma-like spike-timing patterns were one of the intrinsic natures of ongoing information processing within neural circuits.

Discussion

Although spiking-timing patterns are crucial for synaptic plasticity and neural computation, statistical behaviors of spike dynamics across brain-wide regions and multiple animal species were rarely examined. In the present study, we have performed a comprehensive characterization of neuronal spike patterns over a dozen different brain regions in four different animal species. We showed that neuronal spike patterns exhibited positive-skewed, long-tailed distributions. Furthermore, these positive-skewed neuronal spike patterns followed the gamma distribution model. Our analyses provided several detailed insights.

First, according to the independent spike hypothesis that the generation of each spike is independent of all the other spikes, the neuronal spike train would be completely described as a particular kind of random process called Poisson process. If the Poisson process holds true for the neuronal spike-activity patterns, ISI distribution would be statistically described by the exponential distribution model. However, there are certain important features of neuronal firing that may render this simplistic assumption unsatisfactory or inaccurate for capturing spike-time patterns. For example, burst-firing and the refractory periods after the generations of spikes can make neuronal spike patterns deviate away from a Poisson process (exponential distribution model). Indeed, our analysis repeatedly found that spike-time dynamics from 13 brain regions all exhibited the positive-skewed, heavy-tailed distribution that can be best characterized by the gamma distribution model.

Second, previous studies reported that many variables of brain parameters (e.g., firing-rate distributions of neurons, the number of synaptic contacts between neurons, and the size of dendritic boutons) had a positive-skewed, long-tailed distribution - typically

found in log-normal distribution [29, 58]. For example, recent quantifications of cortical principal neurons have shown that the mean firing rates of individual neurons can span at least four orders of magnitude and that the firing-rate distribution of both stimulus-evoked and spontaneous activity in cortical neurons conformed to the log-normal distribution model. While our results support the notion that spike-timing patterns of single neurons followed a positive-skewed distribution, the goodness-of-fit analysis demonstrated that the inter-spike interval of various neurons can be best described by the gamma distribution model. Strikingly, such gamma-distribution statistical patterns are highly conserved across different neuronal types as well as animal species.

Third, despite the fact that neurons' mean firing rates vary between distinct states (shown by the scale parameter θ in the right subpanels of Figures 5A-D), we found that the overall shapes of the neuronal spike patterns are preserved among different states (shown by the scale parameter k in the left subpanels of Figures 5A-D). One hypothesis on this phenomenon is that while the energy level within the neuronal circuit under distinct brain activity states may boost or lessen the mean firing rates, the statistical characteristics of spike-timing patterns are able to remain robust. This preserved statistical characteristic may be determined by preconfigured, skewed synaptic connections and/or intrinsic electrical/chemical attributes of a neuron. This characteristic also offers the potential of estimating a neuron's spike pattern among distinct states. For example, as shown in Figure 5, instead of recording a single neuron's spike train for a long period to get the statistical distribution of its spike pattern in the awake state, one can predict it by using the shape parameter k calculated under the sleep state and/or a mean firing rate within a shorter period in the awake state. Whether this feature holds true for other distinct brain states will require further investigation.

Finally, according to the principle of maximum entropy, a neuronal spike pattern should follow an exponential distribution which indicates a Poisson process. That is, exponential distribution is the maximum entropy distribution among all continuous distributions supported in [0, ∞]. However, instead of showing exponential distribution, the neuronal spike-timing patterns all follow gamma distributions, suggesting a potential knowledge gap between information entropy and information coding. One interesting characteristic is that different brain regions seem to exhibit different degrees of spike irregularities. We found the principal neurons in three brain regions show significantly more regularity in spike-time patterns - namely, DA neurons in the VTA, excitatory principal cells from the somatosensory cortex of the mouse brain, and the monkey parietal area 5d. In contrast, principal neurons in the mouse and cat V1 cortex - as well as principal neurons from the mouse retrosplenial cortex, secondary auditory cortex, anterior cingulate cortex, striatum, amygdala and hippocampal CA1 pyramidal cells - tend to exhibit greater irregularity. Given that internal brain states (such as attention) are known to reduce neuronal variability [59-61], it will be highly interesting to investigate whether such regional variations reflect the underlying molecular and cellular differences (e.g., different cholinergic inputs or receptor expression profiles). In coupling with different NMDA receptor compositions across different regions [62-66], such intrinsic statistical characteristics of spiking-time distribution will likely influence not only how spike-timing patterns drive synaptic plasticity [2, 3], but also how cell assemblies in various circuits perform neural computation [51, 67, 68].

Materials and Methods

Ethics Statement

All animal work described in the study was carried out in accordance with the guidelines laid down by the National Institutes of Health in the United States, regarding the care and use of animals for experimental procedures, and was approved by the Institutional Animal Care and Use Committee of Augusta University (Approval AUP number: BR07-11-001).

Construction of tetrode headstages and animal surgery of the datasets of mouse BLA, CA1, ACC, RSC, STR, V1, 2nd AuV, somatosensory cortex, and hamster PrL

Tetrodes and headstages were constructed using the procedures as we have previously described [51, 69, 70]. To construct tetrodes, a folded piece consisting of four wires (90% platinum, 10% iridium, 13 μm, California Fine Wire Company, Grover Beach, CA, USA) was twisted together using a manual turning device and soldered with a low-intensity heat source (variable temperature heat gun 8977020, Milwaukee, Brookfield, WI, USA) for 6 s. The impedances of the tetrodes were measured with an electrode impedance tester (Model IMP-1, Bak Electronics, Umatilla, FL, USA) to detect any faulty connections, and our tetrodes were typically between 0.7 MΩ and 1 MΩ. The insulation was removed by moving the tips of the free ends of the tetrodes over an open flame for approximately 3 s. The tetrodes were then placed into appropriate polyimide tubes. The recording ends of the tetrodes were cut differentially (Vannas spring scissors −3 mm cutting edge, Fine Science Tools, Foster City, CA, USA) according to the different depths of the recording sites. This ensures that only tetrodes, but not the surrounding polyimide tubes, were inserted into the brain tissue, thereby minimizing the tissue damage.

We employed adjustable 128-channel tetrode microdrives to target the basolateral amygdala (BLA; n = 8 WT mice), hippocampal CA1 (n = 9 WT mice), anterior cingulate cortex (ACC; n = 7 WT mice), the retrosplenial cortex (RSC; n = 20 WT mice), dorsal striatum (STR; n = 7 WT mice), primary visual cortex (V1; n = 14 WT mice), 2nd auditory cortex (2nd AuV; n = 9 WT mice), somatosensory cortex (n = 11 WT mice), and hamster prelimbic region (PrL; n = 13 WT Golden Syrian hamsters) bilaterally with 64 channels per hemisphere [69]. Stereotaxic coordinates were as follows: for BLA, 1.7 mm posterior to bregma, 3.5 mm lateral, −4.0 mm ventral to the brain surface; for ACC, +0.5 mm AP, 0.5 mm ML, −1.75 mm DV; or CA1, 2.0 mm lateral to the bregma and 2.3 posteriors to the bregma; for RSC, −2.5 mm AP, 0.5 mm ML, −0.8 mm DV; for STR, +0.62 mm AP, 1.35 mm ML, −2.0 mm DV; for V1, -3.08 mm AP, 2.5 mm ML, −0.5 mm DV; for 2nd AuV, -1.94 mm AP, 4.75 mm ML; for somatosensory cortex, -1.1 mm AP, 1.5 mm ML; and for recording in the prelimbic cortex (PrL) of the Golden Syrian hamster, the stereotaxic coordinate was +3.50 mm AP, ± 0.7 mm ML, −4.0 mm DV [71].

Male wild-type mice (6–8 months old) or adult male hamsters (3–4 months old) were moved from home cages housed in the LAS facility to the holding area next to the chronic recording rooms in the laboratory and stayed in a large plastic bucket (20 inches in diameter and 16 inches in height per mouse, Walmart) with access to water and food for a week prior to surgery. During this period, the animals were also handled daily to minimize the potential stress from human interaction. On the day of the surgery, the animal was given an intraperitoneal injection of 60 mg/kg ketamine (Bedford Laboratories, Bedford, OH, USA) and 4 mg/kg Domitor (Pfizer, New York, NY, USA) prior to the surgery. The head of the animal was secured in a stereotaxic apparatus, and an ocular lubricant was used to cover the eyes. The hair above the surgery sites was removed, and Betadine solution was applied to the surface of the scalp. An incision was then made along the

midline of the skull. Hydrogen peroxide (3% solution, Fisher Scientific) was placed onto the surface of the skull so that bregma could be visualized. The correct positions for implantation were then measured and marked. For fixing the microdrive headstage, four holes for screws (B002SG89S4, Amazon, Seattle, WA, USA) were drilled on the opposing side of the skull and, subsequently, the screws were placed in these holes with reference wires being secured to two of the head screws. Craniotomies for the tetrode arrays were then drilled, and the dura mater was carefully removed. After the electrodes were inserted and tetrodes were secured to the fiberglass base, the reference wires from the connector-pin arrays were soldered such that there would be a continuous circuit between the ground wires from the head screws and those from the connector-pin arrays. Finally, the connector-pin arrays were coated with epoxy. Aluminum foil was used to surround the entire headstage to aid in the protection and to reduce noise during recordings. The animals were then awoken with an injection of 2.5 mg/kg Antisedan. The animals were allowed to recover post-surgery for at least 3–5 days before recording began. Then, the electrode bundles targeting the BLA, STR and hippocampal CA1 region were slowly advanced over several days in small daily increments. For the cortical sites, tetrodes were advanced usually only once or twice in a small increment. At the end of the experiments, the mice were anesthetized and a small amount of current was applied to the recording electrodes in order to mark the positions of the stereotrode bundles. The actual electrode positions were confirmed by histological Nissl staining using 1% cresyl echt violet. In some experiments, for facilitating the identification of electrode array position, the electrode tips were dipped in fluorescent Neuro-DiI (Neuro-DiI, #60016, Red oily solid color, from Biotium, Inc.) which then can reveal the electrode track.

Experimental Design

We recorded mouse (B6BCA/J) STR, V1, 2nd AuV, somatosensory cortex, and hamster PrL when animals were in the quiet-awake state. The datasets of the mouse (B6BCA/J) ACC, RSC, CA1, and BLA were recorded under two distinct states: the quiet-awake state and sleep state.

In vivo recording of the datasets of mouse BLA, CA1, ACC, RSC, STR, V1, 2nd AuV, somatosensory cortex, and hamster PrL

After surgery, the animals were handled for another 5–10 days while electrodes were advanced to the recording sites for obtaining the maximum neural units.

For the datasets of mouse STR, 2nd AuV, somatosensory cortex, and hamster PrL, recordings were carried out while the animals were in their home cages. Quiet-awake episodes were manually assigned when the mice were awake and immobile. Neuronal spike data during the awake state was recorded for at least 15 minutes for each animal.

For the datasets of mouse ACC, RSC, CA1 and BLA, we recorded the neuronal spike activity in both the quiet-awake state and the sleep state. Recordings were first carried out while the animals were in their home cages. To identify the sleep episodes, local field potentials were first band-pass filtered in theta band (4–12 Hz) and delta band (1–4 Hz); then the ratio of the power in theta band to that of delta band was calculated. Two criteria were applied to extract from the sleep state: (1) Duration of an epoch was longer than 5 s, and (2) the ratio of the power during an epoch was greater than mean 5SD. For each mouse, the awake and sleep states were recorded for at least 15 minutes.

For the dataset of mouse V1, we set up an experimental configuration modified from the design of a previous study [72]. Briefly, a treadmill (5 inches in diameter) was levitated by a stream of pressured air, the tangential force of a mouse running on the

treadmill was calculated to be comparable to the force needed for free running. There was a lick port in front of the mouse's mouth, dropping sugar water every minute. A camera with a telescope was set at the right side of the mouse's eye (8cm distance) for monitoring eye movement. The mouse has implanted electrode arrays in primary visual cortex of the left hemisphere for chronic recording a week before head-fixed visual stimulation experiment. For habituation, the mouse was fixed on the top of a treadmill two hours every day, by mounting the headstage on a metal holder. An optical mouse was placed underneath the treadmill to measure the animal's movements. During the recording, the mouse was to either sit still or run on the treadmill. We found that the eye movement and animal's movement state were highly synchronized, the eyeball was almost fixed when the mouse was in a still state.

Visual stimuli were generated in MATLAB and displayed on a Dell 24-inch monitor placed 27 cm in front of the right eye. Before any recordings, we calibrated the location of the monitor. Specifically, black and white dots with 1-4 degrees were randomly presented on the monitor with a 10 ms duration. The visual responses of the primary visual cortex were amplified, acquired and streamed to the computer by the Plexon electrophysiology recording system. The time stamps of the visual stimulations were also sent to the Plexon simultaneously. The receptive field mapping software was written in MATLAB, which could tag the receptive field of the recorded neurons on the monitor based on the e-Phys data. Then we adjusted the location of the monitor to make sure of the neuron group receptive field to be located in the center of the monitor.

Two different visual stimuli were employed in the formal recording: 1. Full-length drifting bars [combinations of eight orientations (π/8, π/4, π3/8, π/2, π5/8, π3/4, π7/8 and π), four spatial frequencies (0.25, 0.5, 1 and 2 Hz), four temporal frequencies (0.25, 0.5, 1 and 2 Hz) and two directions (drifting either left or right)]; 2. Two-dimensional stimuli [we

recorded 624 gray-scale images of 78 objects (42 toy animals and 36 toy cars), each object was recorded from eight different viewing directions in a 45º interval]. For each recording section, one of these three visual stimuli was delivered. At least 30 minutes of neuronal spike data were recorded during each recording section. Basically, the mice stayed on the treadmill without struggling for more than 2 hours, then we set them free in the home cages.

Cell-type classification in mouse BLA, ACC, RSC, STR, CA1 and hamster PrL

For the datasets recorded from mouse BLA, ACC, RSC, STR, CA1 and hamster PrL, well-isolated units were classified as either putative excitatory principal cells or inhibitory interneurons based on three characteristic features of their spike activities - namely, trough-to-peak width, half-width after trough, and the mean firing rates. The k-means method was employed to achieve automated cell-type clustering. In general, putative principal cells fire at lower rates and have broader waveforms, whereas interneurons have higher rates and relatively narrower waveforms.

Animal surgery and *in vivo* recording of mouse VTA dataset

The details have been previously described [38]. A 32-channel (a bundle of eight tetrodes) electrode array was constructed. One week before surgery, mice (3–6 months old) were removed from the standard cages and housed in customized home cages (40×20×25 cm). On the day of surgery, the mice were anesthetized with Ketamine/Xylazine (80/12 mg/kg, i.p.); the electrode array was then implanted toward the VTA in the right hemisphere (3.4 mm posterior to bregma, 0.5 mm lateral and 3.8–4.0 mm ventral to the brain surface) and secured with dental cement.

Two or three days after surgery, the electrodes were screened daily for neural activity. If no dopamine neurons were detected, the electrode array was advanced 40~100

µm daily, until we could record from a putative dopamine neuron. In brief, spikes (filtered at 250–8000 Hz; digitized at 40 kHz) were recorded during the entire experimental process using the Plexon multichannel acquisition processor system (Plexon Inc.). Mice behaviors were simultaneously recorded using the Plexon CinePlex tracking system. Recorded spikes were isolated using Plexon OfflineSorter software. Dopamine neurons were distinguished from other neurons in the region by the characteristics of their extracellularly recorded impulses - including long, multiphasic waveforms and low basal firing rates.

Fearful-event experiment

Mice were subjected to three fearful episodic events - earthquakes, footshocks and free-fall drops. For the earthquake-like shake, the mouse was placed in a small chamber (4" x 4" x 6"H circular chamber) fixed on top of a vortex mixer and shaken at 300 rpm for 400ms six times with a 1~3-minute time interval between each shake. For fearful footshock, the footshock chamber was a square chamber (10" × 10" × 15"H) with a 24-bar shock grid floor. The mouse was placed into the shock chamber for three minutes and received the footshock stimulus (a continuous 300-ms footshock at 0.75 mA) for a total of six times with inter-trial time intervals between 1~3 minutes. For free-fall in the elevator, the animal was placed inside a small box (3" x 3" x 5"H) and dropped from a 13-cm height (a cushion made from a crumbled tablecloth was used to dampen the fall and to stop the bouncing effect). After 1~2 minutes, the elevator was raised gently back to the 13-cm height and dropped again after 1~2 minutes (this process was also repeated six times). These episodic stimuli are fearful as evidenced from physiological indications including a rapid increase in heart rates as well as reduced heart-rate variability [73, 74]. To maintain the consistency of stimulation timing (minimizing the possible prediction of upcoming stimuli), the stimuli were triggered by a computer and delivered at randomized intervals

within 1-3 minutes. After the completion of all fearful event sessions, the mouse was placed back into the home cage.

Dataset recorded from the quiet-awake state and anesthesia

Three datasets were recorded from BLA, hippocampal CA1, and RSC under two distinct states - namely the quiet-awake state and anesthesia. Recordings were first carried out when animals were awake and immobile in their home cages. Minimum 40-minute neural activities were recorded under the quiet-awake state. To produce ketamine-induced anesthesia, the animals were injected with a 60 mg/kg ketamine and 0.5 mg/kg Domitor cocktail mixture via *i.p.*, the animals lost the righting reflex in a few minutes. Neural spike activities were recorded for 50 minutes under the anesthetized state. Forty-minute neural spike data recorded from the fully anesthetized state starting from 10 minutes after the Ketamine/Domitor injections were selected for the present analysis. The dataset for neuronal variability analyses of awake state vs. anesthesia (Figure 14) contained 92 BLA putative principal cells from two mice, 59 CA1 putative principal cells from 3 mice, and 59 RSC putative principal cells from 3 mice.

Monkey area 5d dataset

The dataset was previously described [75]. Data were recorded from two male rhesus monkeys (Macaca mulatta, 7-10 kg). The animals were trained to perform visually guided single- and double-arm reaching tasks. All procedures were in accordance with NIH guidelines and were approved by the Institutional Animal Care and Use Committee of Augusta University. Recorded spikes were re-sorted using Plexon OfflineSorter software for obtaining the spike trains of single neurons; multiple spike-sorting parameters (e.g., principal component analysis, energy analysis) were used for the best isolation of single-unit spike trains. Because of the absence of the spike waveform information, we were not able to separate different neuron types (excitatory vs. inhibitory cells, etc.).

However, we observed at the conclusion that neuronal spike activities that can best be described by the gamma distribution model still hold true in the monkey area 5d region.

Cat V1 Datasets

The cat V1 datasets (1-D and 2-D) were downloaded from the Collaborative Research in Computational Neuroscience (CRCNS) website (data from Yang Dan Lab at UC-Berkeley, download link: http://crcns.org/data-sets/vc/pvc-2). Experimental procedures have been previously described [55-57]. The data were obtained with extracellular recordings from the primary visual cortex of anesthetized adult cats. Single-unit recordings were made in area 17 of adult cats (2–6.5 kg) using tungsten electrodes (A-M Systems, Carlsborg, WA). Animals were initially anesthetized with isoflurane (3%, with O_2) followed by sodium pentothal (10 mg/kg, i.v., supplemented as needed). During recording, anesthesia was maintained with sodium pentothal (3 $mg \cdot kg^{-1} \cdot hr^{-1}$, i.v.), and paralysis was maintained with pancuronium bromide (0.1–0.2 $mg \cdot kg^{-1} \cdot hr^{-1}$, i.v.). Because of the absence of the spike waveform information, we were not able to separate different neuron types (excitatory vs. inhibitory cells, etc.). However, we observed at the conclusion that neuronal spike activities that can best be described by the gamma distribution model still hold true in cat V1 region (both 1-D and 2-D stimuli).

Data processing and spike-sorting

Neuronal activities from mouse experiments were recorded by the MAP system (multi-channel acquisition processor system, Plexon Inc., Dallas, TX) in the manner as previously described [76]. Extracellular action potentials and local field potentials data were recorded simultaneously and digitized at 40 kHz and 1 kHz, respectively. The artifact waveforms were removed and the spike waveform minima were aligned using the Offline Sorter 2.0 software (Plexon Inc., Dallas, TX), which resulted in more tightly clustered waveforms in principal component space. Spike sortings were done with the MClust 3.3

program with an auto-clustering method (KlustaKwik 1.5). Only units with clear boundaries and less than 0.5% of spike intervals within a 1 ms refractory period were selected. The stability of the *in vivo* recordings was judged by waveforms at the beginning, during and after the experiments. Well-separated neurons were assessed by "Isolation Distance" [35]. Neurons whose "Isolation Distance" >15 were selected for the present analysis as previously described [51, 69, 70].

Statistical Analysis

As shown in Figure 5, a *t*-test was used to assess whether k (or θ) were linearly correlated between the quiet-awake state and the sleep state. In Figure 11, one-way ANOVA analysis and Tukey post hoc tests were conducted for the comparisons of multiple means of k across different brain regions. Three asterisks denoted the p-value is less than 0.001. Data were represented as mean ± SEM.

Statistical properties of neural spike patterns

A two-step analysis was employed to examine the statistical properties of neural spike patterns.

Step 1: Positive-skewed vs. negative-skewed distributions. The distribution of ISI was characterized by two well-defined statistics - namely, nonparametric-skew (S) and skewness (γ), defined as follows:

$$S = \frac{\mu - \upsilon}{\sigma} \tag{1}$$

$$\gamma = \mathrm{E}\left[\left(\frac{I-\mu}{\sigma}\right)^3\right] = \frac{\mathrm{E}\left[(I-\mu)^3\right]}{\left(\mathrm{E}\left[(I-\mu)^2\right]\right)^{3/2}} \tag{2}$$

where μ is the mean, υ is the median, σ is the standard deviation, E is the expectation operator, and I denotes the ISIs of a neuronal spike train.

In probability theory and statistics, nonparametric-skew (S) and skewness [$\gamma \in (-\infty, +\infty)$] are measurements of the skewness (or long-tailedness) of a random variable's distribution – that is, the distribution's tendency to lean to one side or the other of the mean (Figure 1B). A positive-skewed distribution (red curve in Figure 1B) has $S > 0$ and $\gamma > 0$, a negative-skewed distribution (blue curve in Figure 1B) has $S < 0$ and $\gamma < 0$, while a symmetric distribution (gray dotted curves in Figure 1B) has $S = 0$ and $\gamma = 0$.

Step 2: Gamma distribution vs. log-normal distribution. Let $I_1, I_2, \cdots I_n$ denote the ISIs of a neuron's spike train; the probability density function for a gamma distribution of I is defined by a shape parameter $k > 0$ and a scale parameter $\theta > 0$:

$$f_{GA}(i; k, \theta) = \frac{1}{\Gamma(k)\theta^k} i^{k-1} e^{-\frac{i}{\theta}} \tag{3}$$

where $\Gamma(k)$ is the gamma function.

The probability density function of a log-normal distribution of I is defined by a location parameter $\mu \in (-\infty, +\infty)$ and a scale parameter $\sigma > 0$:

$$f_{LN}(i; \mu, \sigma) = \frac{1}{\sqrt{2\pi} i\sigma} e^{-\frac{(\ln i - \mu)^2}{2\sigma^2}} \tag{4}$$

In the present analyses, both gamma distribution and log-normal distribution were estimated using the maximum likelihood estimates (MLE) method, which selected values of parameters that produced corresponding distributions for the histograms of ISI with

minimal errors. The parameters of both gamma distribution and log-normal distribution were directly estimated by using the raw ISIs of neuronal spike activities, which ensured that the analyses of ISI distributions were independent of the bin sizes used.

Goodness-of-fit analyses were then conducted to quantitatively discriminate between the gamma distribution and log-normal distribution models. For convenience, we termed a gamma distribution and a log-normal distribution as $GA(k,\theta)$ and $LN(\mu,\sigma)$, respectively. Thus, the likelihood functions of data that follow $GA(k,\theta)$ and $LN(\mu,\sigma)$ can be denoted as:

$$L_{GA}(k,\theta)=\prod_{j=1}^{n} f_G\left(i;k,\theta\right) \tag{5}$$

$$L_{LN}(\mu,\sigma)=\prod_{j=1}^{n} f_{LN}\left(i;\mu,\sigma\right) \tag{6}$$

Therefore, the RML between a gamma distribution and a log-normal distribution is defined as:

$$RML=\frac{L_{GA}(\hat{k},\hat{\theta})}{L_{LN}(\hat{\mu},\hat{\sigma})} \tag{7}$$

where $(\hat{k},\hat{\theta})$ and $(\hat{\mu},\hat{\sigma})$ are the MLEs of (k,θ) and (μ,σ) for I. The natural logarithm of RML can be written as:

$$D=n\left[\hat{k}\ln\left(\frac{\tilde{I}}{\hat{\theta}}\right)+\frac{1}{2\hat{\sigma}^2 n}\sum_{j=1}^{n}\left(\ln\left(\frac{I_j}{\hat{\mu}}\right)\right)^2+\frac{1}{2}\ln\left(2\pi\right)-\ln\left(\frac{\Gamma\left(\hat{k}\right)}{\hat{\sigma}}\right)-\frac{\bar{I}}{\hat{\theta}}\right] \tag{8}$$

where $\overline{I} = \frac{1}{n}\sum_{j=1}^{n} I_j$ and $\tilde{I} = \left(\prod_{j=1}^{n} I_j\right)^{\frac{1}{n}}$ are the arithmetic and geometric means of I, respectively.

The natural logarithm of RML, D, measured the goodness-of-fit between the gamma distribution model and the log-normal distribution model of ISI. That is, the gamma distribution model precedes the log-normal distribution model if $D > 0$; otherwise, choose the log-normal distribution as the preferred model of ISI. The larger the absolute value of D, the more accurate-fitting the result of the chosen model over the other model.

Author Contributions: J.Z.T. and M.L. conceived and designed the project. J.Z.T. designed the experiments with M.L., K.X., H.K., G.E.F. and J.L. The research was performed as follows: K.X. recorded from the ACC and PrL datasets; G.E.F. from the RSC; Jun Liu from the BLA; D.W. from the striatum, H.K. for the CA1, M.L., F.Z., Z.S., L.C., Y.M., and H.K. for data analyses together with J.Z.T. J.Z.T. and M.L. wrote the paper with input from all others.

Conflict of Interest: The authors declare no competing financial interests.

Acknowledgements: This work is supported by an NIH grant (R01NS079774) and GRA equipment grant to J.Z.T., Shanghai Youth Science and Technology Sail Project (16YF1415200) to Z.S. and M.L., the Brain Decoding Center grant Yunnan Science Commission (2014DG002) to F.Z. and J.Z.T. We thank Prof. Yang Dan at UC Berkeley for sharing the cat dataset, which was downloaded from the CRCNS website. We thank Sandra E. Jackson for proofreading the manuscript.

References

1. Sjostrom PJ, Turrigiano GG, Nelson SB. Rate, timing, and cooperativity jointly determine cortical synaptic plasticity. Neuron. 2001;32(6):1149-64.

2. Lisman J, Spruston N. Postsynaptic depolarization requirements for LTP and LTD: a critique of spike timing-dependent plasticity. Nat Neurosci. 2005;8(7):839-41.

3. Song S, Miller KD, Abbott LF. Competitive Hebbian learning through spike-timing-dependent synaptic plasticity. Nat Neurosci. 2000;3(9):919-26.

4. Markram H, Lubke J, Frotscher M, Sakmann B. Regulation of synaptic efficacy by coincidence of postsynaptic APs and EPSPs. Science. 1997;275(5297):213-5.

5. Gerstner W, Kempter R, van Hemmen JL, Wagner H. A neuronal learning rule for sub-millisecond temporal coding. Nature. 1996;383(6595):76-81.

6. deCharms RC, Zador A. Neural representation and the cortical code. Annu Rev Neurosci. 2000;23:613-47.

7. Brown EN, Kass RE, Mitra PP. Multiple neural spike train data analysis: state-of-the-art and future challenges. Nat Neurosci. 2004;7(5):456-61.

8. Shadlen MN, Newsome WT. Noise, neural codes and cortical organization. Curr Opin Neurobiol. 1994;4(4):569-79.

9. Faisal AA, Selen LP, Wolpert DM. Noise in the nervous system. Nat Rev Neurosci. 2008;9(4):292-303.

10. Masquelier T. Neural variability, or lack thereof. Front Comput Neurosci. 2013;7:7.

11. Ermentrout GB, Galan RF, Urban NN. Reliability, synchrony and noise. Trends Neurosci. 2008;31(8):428-34.

12. Abbott L, Sejnowski TJ. Neural codes and distributed representations: foundations of neural computation: Mit Press; 1999.

13. Mainen ZF, Sejnowski TJ. Reliability of spike timing in neocortical neurons. Science. 1995;268(5216):1503-6.

14. Toups JV, Fellous J-M, Thomas PJ, Sejnowski TJ, Tiesinga PH. Multiple spike time patterns occur at bifurcation points of membrane potential dynamics. PLoS Comput Biol. 2012;8(10):e1002615.

15. Gerstner W, Naud R. Neuroscience. How good are neuron models? Science. 2009;326(5951):379-80.

16. Ma WJ, Beck JM, Latham PE, Pouget A. Bayesian inference with probabilistic population codes. Nature neuroscience. 2006;9(11):1432-8.

17. Mazurek ME, Shadlen MN. Limits to the temporal fidelity of cortical spike rate signals. Nature neuroscience. 2002;5(5):463-71.

18. Shadlen MN, Newsome WT. The variable discharge of cortical neurons: implications for connectivity, computation, and information coding. Journal of neuroscience. 1998;18(10):3870-96.

19. Gilson M, Masquelier T, Hugues E. STDP allows fast rate-modulated coding with Poisson-like spike trains. PLoS Comput Biol. 2011;7(10):e1002231.

20. Caporale N, Dan Y. Spike timing-dependent plasticity: a Hebbian learning rule. Annu Rev Neurosci. 2008;31:25-46.

21. Moezzi B, Iannella N, McDonnell MD. Ion channel noise can explain firing correlation in auditory nerves. J Comput Neurosci. 2016;41(2):193-206.

22. Kang J, Wu J, Smerieri A, Feng J. Weber's law implies neural discharge more regular than a Poisson process. The European journal of neuroscience. 2010;31(6):1006-18.

23. Heil P, Neubauer H, Irvine DRF, Brown M. Spontaneous activity of auditory-nerve fibers: insights into stochastic processes at ribbon synapses. Journal of neuroscience. 2007;27(31):8457-74.

24. Lindner B. Superposition of many independent spike trains is generally not a Poisson process. Physical Review E. 2006;73(2):022901.

25. Kara P, Reinagel P, Reid RC. Low response variability in simultaneously recorded retinal, thalamic, and cortical neurons. Neuron. 2000;27(3):635-46.

26. DeWeese MR, Wehr M, Zador AM. Binary spiking in auditory cortex. Journal of neuroscience. 2003;23(21):7940-9.

27. Li M, Zhao F, Lee J, Wang D, Kuang H, Tsien JZ. Computational Classification Approach to Profile Neuron Subtypes from Brain Activity Mapping Data. Sci Rep. 2015;5:12474.

28. Berkes P, Orban G, Lengyel M, Fiser J. Spontaneous cortical activity reveals hallmarks of an optimal internal model of the environment. Science. 2011;331(6013):83-7.

29. Mizuseki K, Buzsaki G. Preconfigured, skewed distribution of firing rates in the hippocampus and entorhinal cortex. Cell Rep. 2013;4(5):1010-21.

30. Maimon G, Assad JA. Beyond Poisson: increased spike-time regularity across primate parietal cortex. Neuron. 2009;62(3):426-40.

31. Pipa G, Grun S, van Vreeswijk C. Impact of spike train autostructure on probability distribution of joint spike events. Neural Comput. 2013;25(5):1123-63.

32. Cox DR, editor Tests of separate families of hypotheses. Proceedings of the fourth Berkeley symposium on mathematical statistics and probability; 1961.

33. Cox DR. Further results on tests of separate families of hypotheses. Journal of the Royal Statistical Society Series B (Methodological). 1962:406-24.

34. Cox DR. A return to an old paper:'Tests of separate families of hypotheses'. Journal of the Royal Statistical Society: Series B (Statistical Methodology). 2013;75(2):207-15.

35. Schmitzer-Torbert N, Jackson J, Henze D, Harris K, Redish AD. Quantitative measures of cluster quality for use in extracellular recordings. Neuroscience. 2005;131(1):1-11.

36. Preston RJ, Bishop GA, Kitai ST. Medium spiny neuron projection from the rat striatum: an intracellular horseradish peroxidase study. Brain Res. 1980;183(2):253-63.

37. Surmeier DJ, Ding J, Day M, Wang Z, Shen W. D1 and D2 dopamine-receptor modulation of striatal glutamatergic signaling in striatal medium spiny neurons. Trends Neurosci. 2007;30(5):228-35.

38. Wang DV, Tsien JZ. Convergent processing of both positive and negative motivational signals by the VTA dopamine neuronal populations. PloS one. 2011;6(2):e17047.

39. Lammel S, Ion DI, Roeper J, Malenka RC. Projection-specific modulation of dopamine neuron synapses by aversive and rewarding stimuli. Neuron. 2011;70(5):855-62.

40. Beier KT, Steinberg EE, DeLoach KE, Xie S, Miyamichi K, Schwarz L, et al. Circuit Architecture of VTA Dopamine Neurons Revealed by Systematic Input-Output Mapping. Cell. 2015;162(3):622-34.

41. Swanson LW. The projections of the ventral tegmental area and adjacent regions: a combined fluorescent retrograde tracer and immunofluorescence study in the rat. Brain Res Bull. 1982;9(1-6):321-53.

42. Bromberg-Martin ES, Matsumoto M, Hikosaka O. Dopamine in motivational control: rewarding, aversive, and alerting. Neuron. 2010;68(5):815-34.

43. Schultz W. Updating dopamine reward signals. Current opinion in neurobiology. 2013;23(2):229-38.

44. Everitt BJ, Robbins TW. Neural systems of reinforcement for drug addiction: from actions to habits to compulsion. Nat Neurosci. 2005;8(11):1481-9.

45. Wise RA. Dopamine, learning and motivation. Nat Rev Neurosci. 2004;5(6):483-94.

46. Berridge KC, Robinson TE, Aldridge JW. Dissecting components of reward: 'liking', 'wanting', and learning. Curr Opin Pharmacol. 2009;9(1):65-73.

47. Grace AA. The tonic/phasic model of dopamine system regulation and its implications for understanding alcohol and psychostimulant craving. Addiction. 2000;95 Suppl 2:S119-28.

48. Abraham AD, Neve KA, Lattal KM. Dopamine and extinction: a convergence of theory with fear and reward circuitry. Neurobiol Learn Mem. 2014;108:65-77.

49. Fadok JP, Dickerson TMK, Palmiter RD. Dopamine is necessary for cue-dependent fear conditioning. Journal of neuroscience. 2009;29(36):11089-97.

50. Pezze MA, Feldon J. Mesolimbic dopaminergic pathways in fear conditioning. Prog Neurobiol. 2004;74(5):301-20.

51. Xie K, Fox GE, Liu J, Lyu C, Lee JC, Kuang H, et al. Brain Computation Is Organized via Power-of-Two-Based Permutation Logic. Front Syst Neurosci. 2016;10:95.

52. Hamel-Pâquet C, Sergio LE, Kalaska JF. Parietal area 5 activity does not reflect the differential time-course of motor output kinetics during arm-reaching and isometric-force tasks. J Neurophysiol. 2006;95(6):3353-70.

53. Cui H, Andersen RA. Different representations of potential and selected motor plans by distinct parietal areas. Journal of neuroscience. 2011;31(49):18130-6.

54. Dan Y, Felsen G, Touryan J. Extracellular recording from cells in cat primary visual cortex. CRCNSorg. 2009.

55. Felsen G, Touryan J, Han F, Dan Y. Cortical sensitivity to visual features in natural scenes. PLoS Biol. 2005;3(10):e342.

56. Touryan J, Felsen G, Dan Y. Spatial structure of complex cell receptive fields measured with natural images. Neuron. 2005;45(5):781-91.

57. Touryan J, Lau B, Dan Y. Isolation of relevant visual features from random stimuli for cortical complex cells. Journal of neuroscience. 2002;22(24):10811-8.

58. Buzsaki G, Mizuseki K. The log-dynamic brain: how skewed distributions affect network operations. Nat Rev Neurosci. 2014;15(4):264-78.

59. Cohen MR, Maunsell JHR. Attention improves performance primarily by reducing interneuronal correlations. Nat Neurosci. 2009;12(12):1594-600.

60. Mitchell JF, Sundberg KA, Reynolds JH. Spatial attention decorrelates intrinsic activity fluctuations in macaque area V4. Neuron. 2009;63(6):879-88.

61. Mitchell JF, Sundberg KA, Reynolds JH. Differential attention-dependent response modulation across cell classes in macaque visual area V4. Neuron. 2007;55(1):131-41.

62. Tang YP, Shimizu E, Dube GR, Rampon C, Kerchner GA, Zhuo M, et al. Genetic enhancement of learning and memory in mice. Nature. 1999;401(6748):63-9.

63. Cui Z, Feng R, Jacobs S, Duan Y, Wang H, Cao X, et al. Increased NR2A:NR2B ratio compresses long-term depression range and constrains long-term memory. Sci Rep. 2013;3:1036.

64. Jacobs S, Cui Z, Feng R, Wang H, Wang D, Tsien JZ. Molecular and genetic determinants of the NMDA receptor for superior learning and memory functions. PloS one. 2014;9(10):e111865.

65. Sheng M, Cummings J, Roldan LA, Jan YN, Jan LY. Changing subunit composition of heteromeric NMDA receptors during development of rat cortex. Nature. 1994;368(6467):144-7.

66. Monyer H, Sprengel R, Schoepfer R, Herb A, Higuchi M, Lomeli H, et al. Heteromeric NMDA receptors: molecular and functional distinction of subtypes. Science. 1992;256(5060):1217-21.

67. Gupta AS, van der Meer MA, Touretzky DS, Redish AD. Hippocampal replay is not a simple function of experience. Neuron. 2010;65(5):695-705.

68. Buzsaki G. Neural syntax: cell assemblies, synapsembles, and readers. Neuron. 2010;68(3):362-85.

69. Lin L, Chen G, Xie K, Zaia KA, Zhang S, Tsien JZ. Large-scale neural ensemble recording in the brains of freely behaving mice. J Neurosci Methods. 2006;155(1):28-38.

70. Xie K, Fox GE, Liu J, Tsien JZ. 512-Channel and 13-Region Simultaneous Recordings Coupled with Optogenetic Manipulation in Freely Behaving Mice. Front Syst Neurosci. 2016;10:48.

71. Paxinos G, Franklin KB. The mouse brain in stereotaxic coordinates: Gulf Professional Publishing; 2004.

72. Niell CM, Stryker MP. Modulation of visual responses by behavioral state in mouse visual cortex. Neuron. 2010;65(4):472-9.

73. Liu J, Wei W, Kuang H, Tsien JZ, Zhao F. Heart rate and heart rate variability assessment identifies individual differences in fear response magnitudes to earthquake, free fall, and air puff in mice. PLoS One. 2014;9(3):e93270.

74. Liu J, Wei W, Kuang H, Zhao F, Tsien JZ. Changes in heart rate variability are associated with expression of short-term and long-term contextual and cued fear memories. PLoS One. 2013;8(5):e63590.

75. Li Y, Cui H. Dorsal parietal area 5 encodes immediate reach in sequential arm movements. Journal of neuroscience. 2013;33(36):14455-65.

76. Kuang H, Lin L, Tsien JZ. Temporal dynamics of distinct CA1 cell populations during unconscious state induced by ketamine. PLoS One. 2010;5(12):e15209.

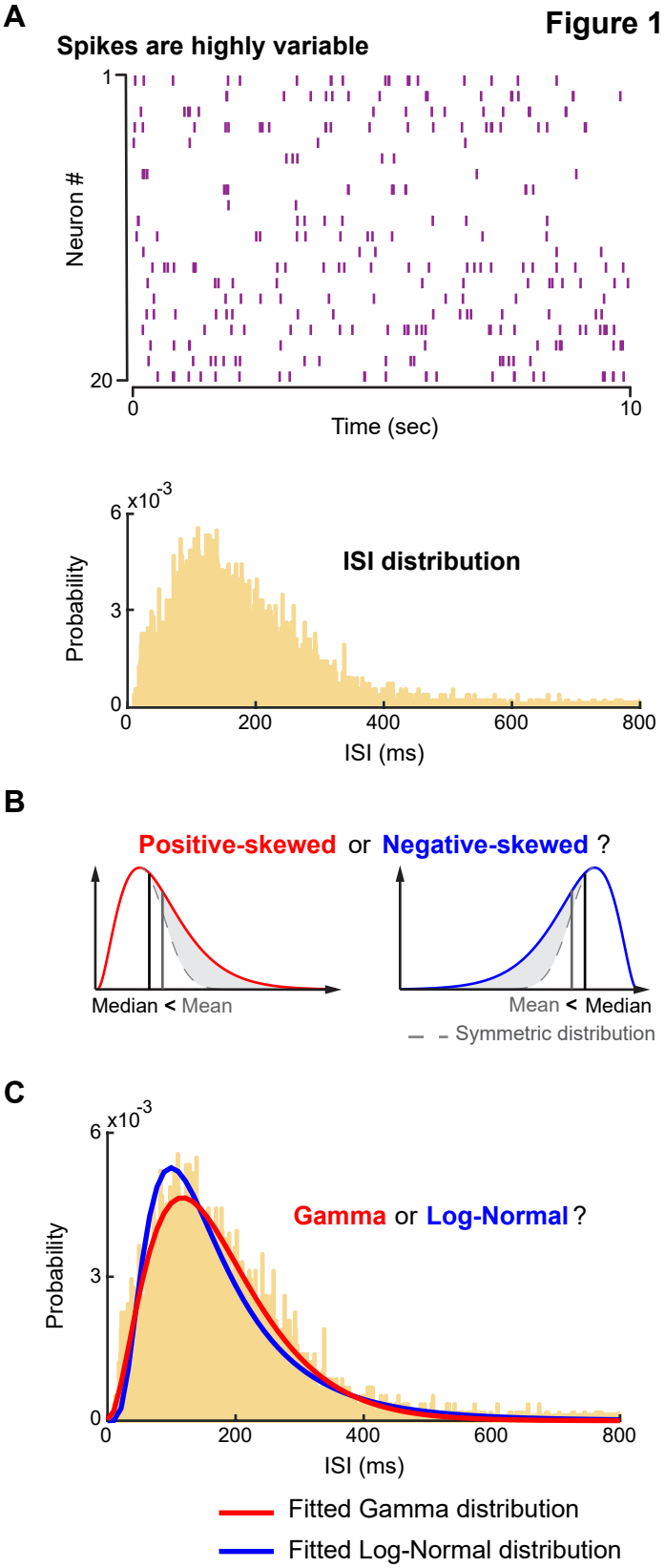
A
Figure 1
Spikes are highly variable
Neuron #
1
20
0
10
Time (sec)
x10^-3
6
3
0
Probability
ISI distribution
0
200
400
600
800
ISI (ms)
B
Positive-skewed or Negative-skewed ?
Median < Mean
Mean < Median
Symmetric distribution
C
x10^-3
6
3
0
Probability
Gamma or Log-Normal ?
0
200
400
600
800
ISI (ms)
Fitted Gamma distribution
Fitted Log-Normal distribution

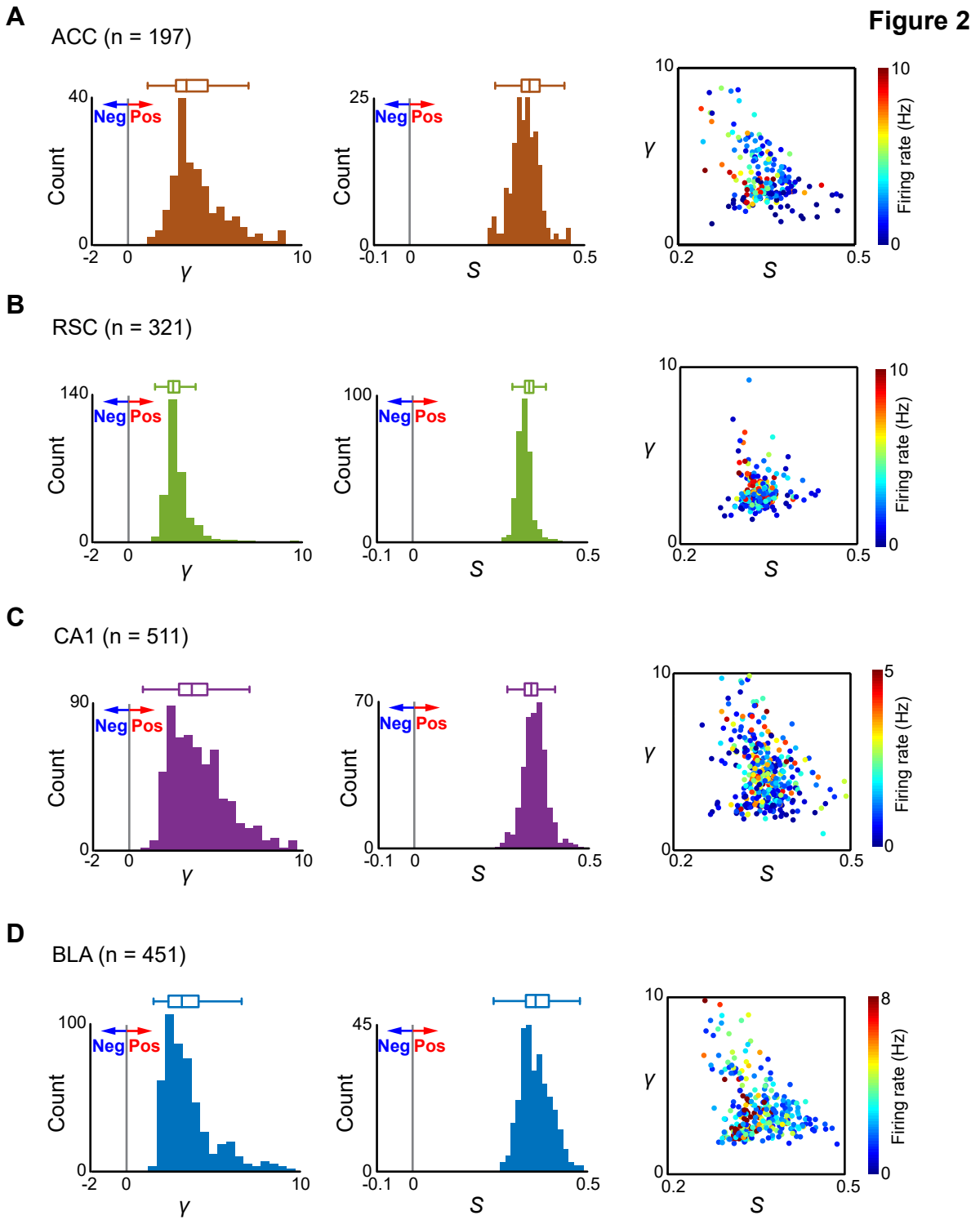
Figure 2
A
ACC (n = 197)
B
RSC (n = 321)
C
CA1 (n = 511)
D
BLA (n = 451)
Neg
Pos
Count
γ
S
Firing rate (Hz)

Figure 3

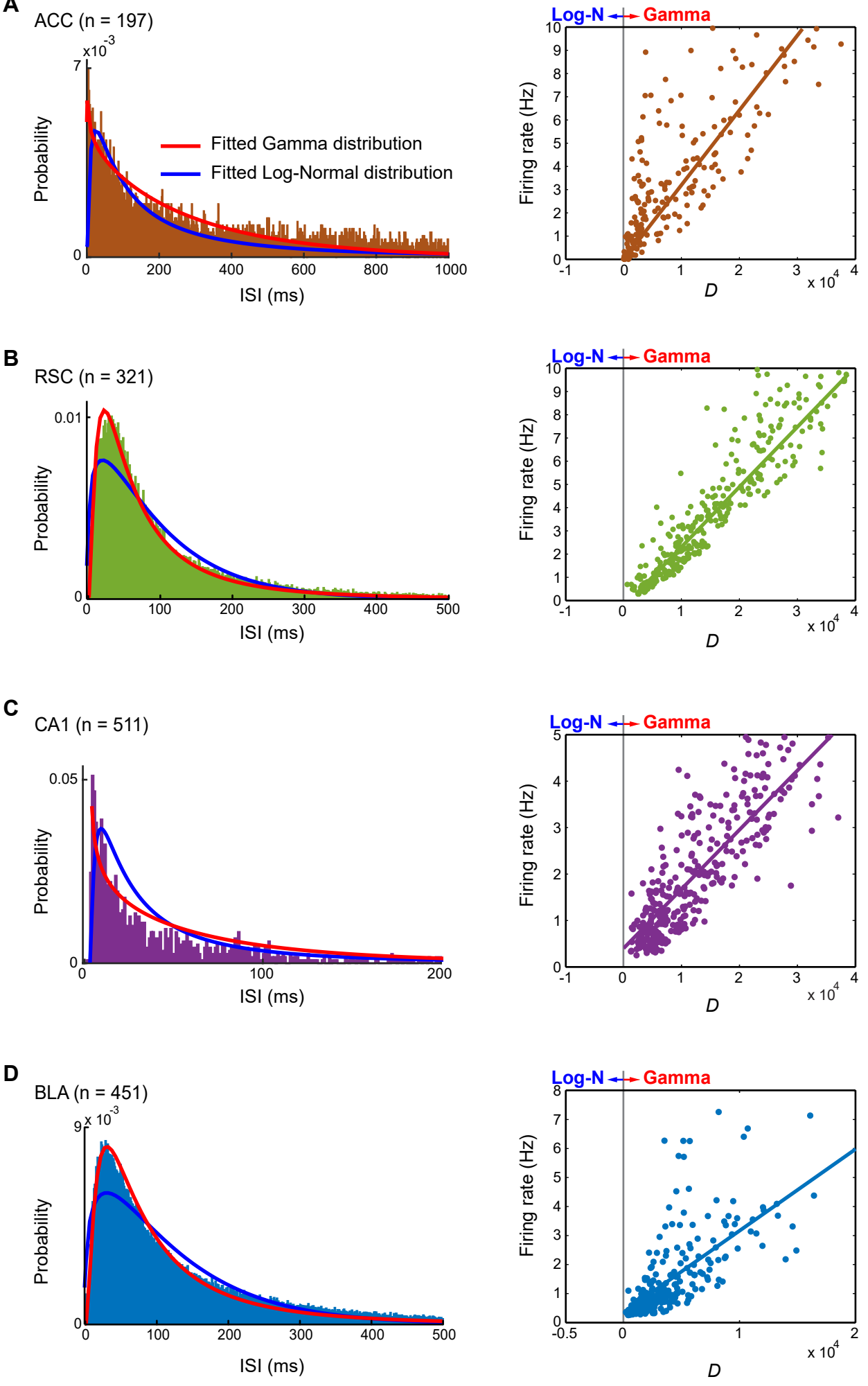
A
ACC (n = 197)
x10^-3
Probability
Fitted Gamma distribution
Fitted Log-Normal distribution
ISI (ms)
Log-N ← → Gamma
Firing rate (Hz)
D
x 10^4
B
RSC (n = 321)
Probability
ISI (ms)
Log-N ← → Gamma
Firing rate (Hz)
D
x 10^4
C
CA1 (n = 511)
Probability
ISI (ms)
Log-N ← → Gamma
Firing rate (Hz)
D
x 10^4
D
BLA (n = 451)
x 10^-3
Probability
ISI (ms)
Log-N ← → Gamma
Firing rate (Hz)
D
x 10^4

Figure 4

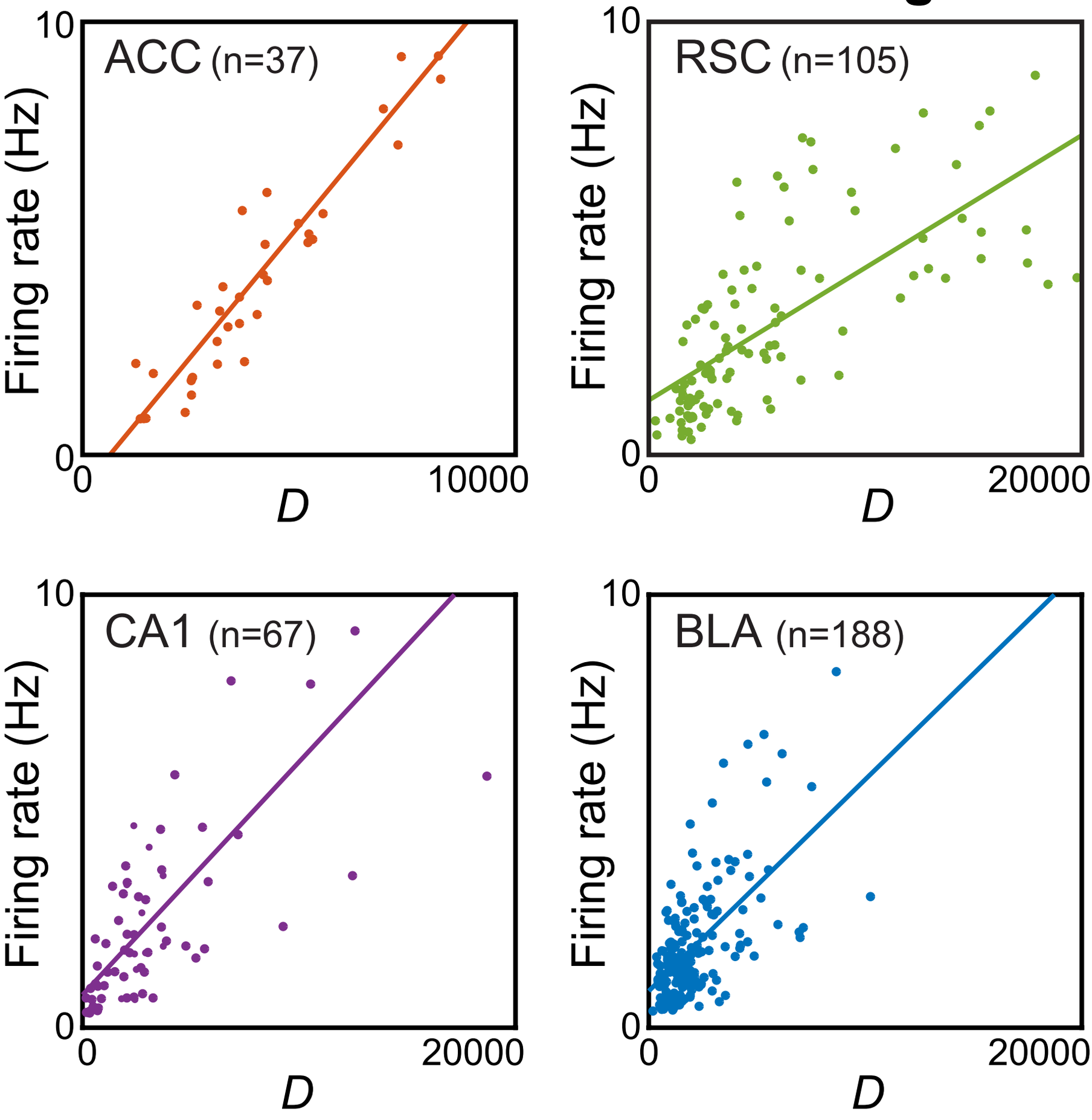
ACC (n=37)
RSC (n=105)
CA1 (n=67)
BLA (n=188)
Firing rate (Hz)
D
10
0
0
10000
20000

Figure 5

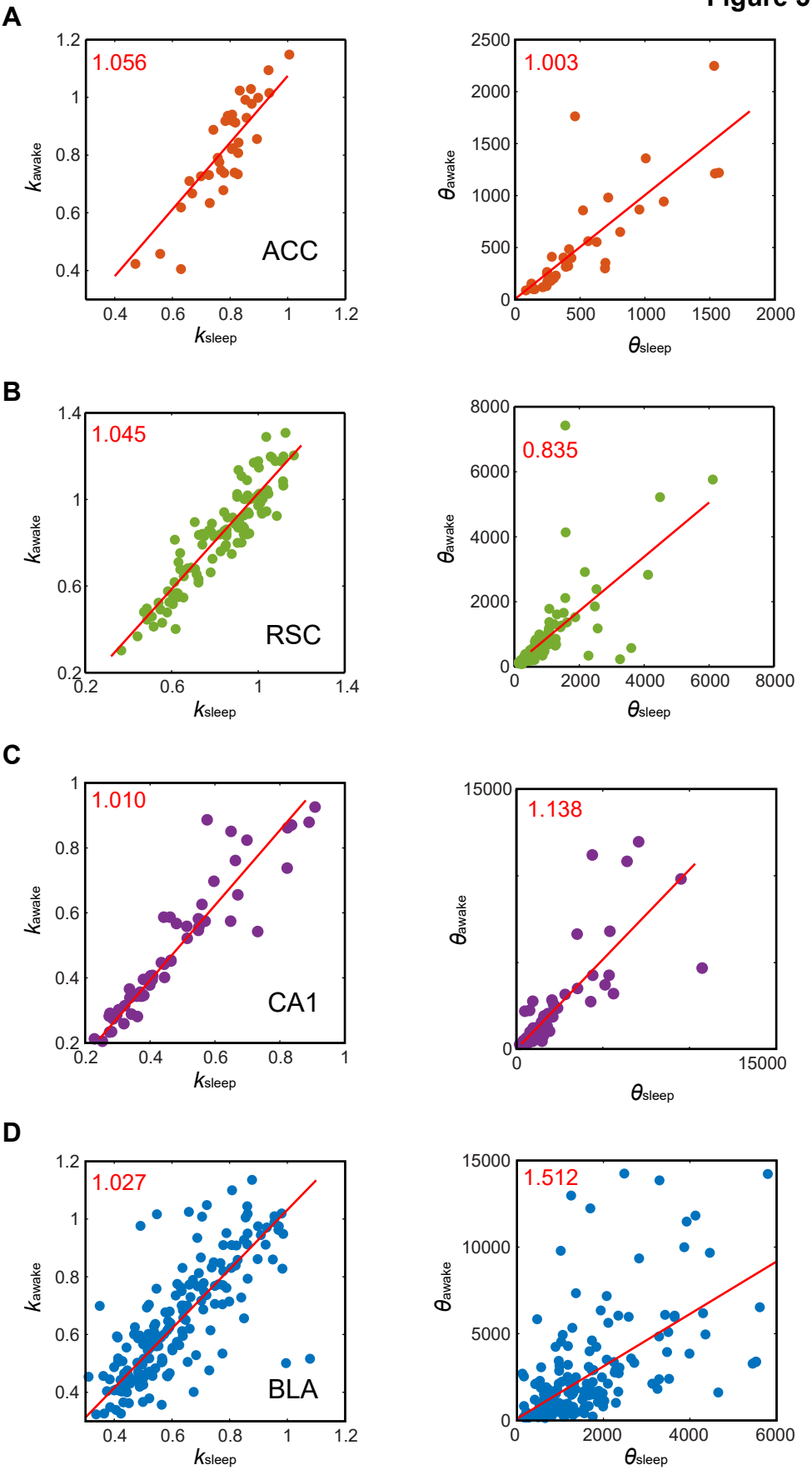
A
1.056
ACC
k_{awake}
k_{sleep}
1.003
θ_{awake}
θ_{sleep}
B
1.045
RSC
k_{awake}
k_{sleep}
0.835
θ_{awake}
θ_{sleep}
C
1.010
CA1
k_{awake}
k_{sleep}
1.138
θ_{awake}
θ_{sleep}
D
1.027
BLA
k_{awake}
k_{sleep}
1.512
θ_{awake}
θ_{sleep}

Figure 6

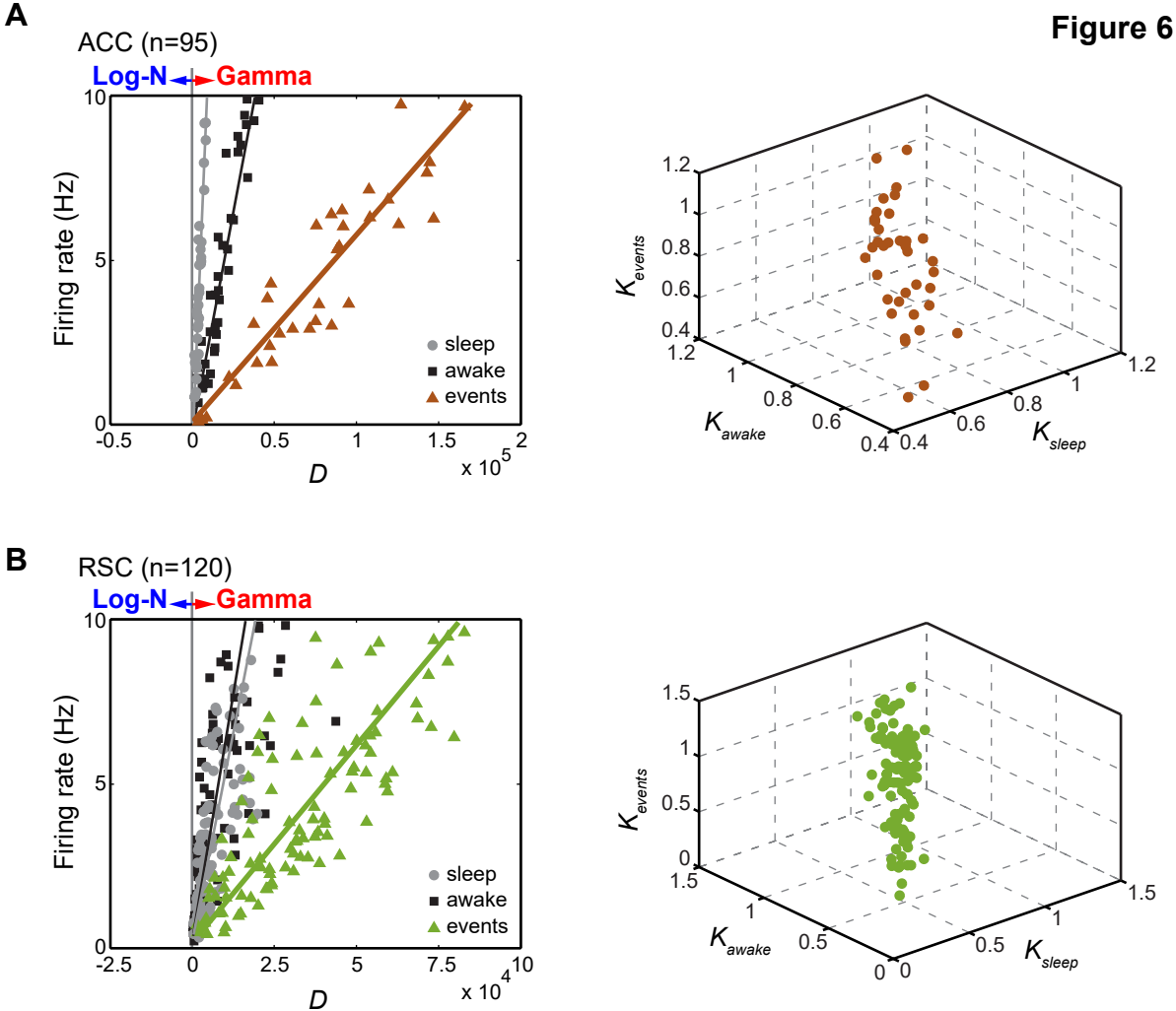
A
ACC (n=95)
Log-N
Gamma
Firing rate (Hz)
D
x 10^5
sleep
awake
events
K_events
K_awake
K_sleep
B
RSC (n=120)
Log-N
Gamma
Firing rate (Hz)
D
x 10^4
sleep
awake
events
K_events
K_awake
K_sleep

Figure 7

A

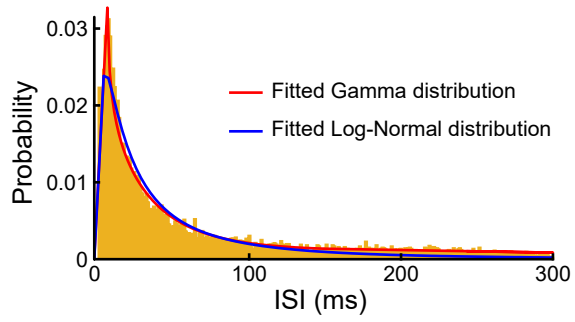
Striatum
Probability
0.03
0.02
0.01
0
Fitted Gamma distribution
Fitted Log-Normal distribution
0
100
200
300
ISI (ms)

B

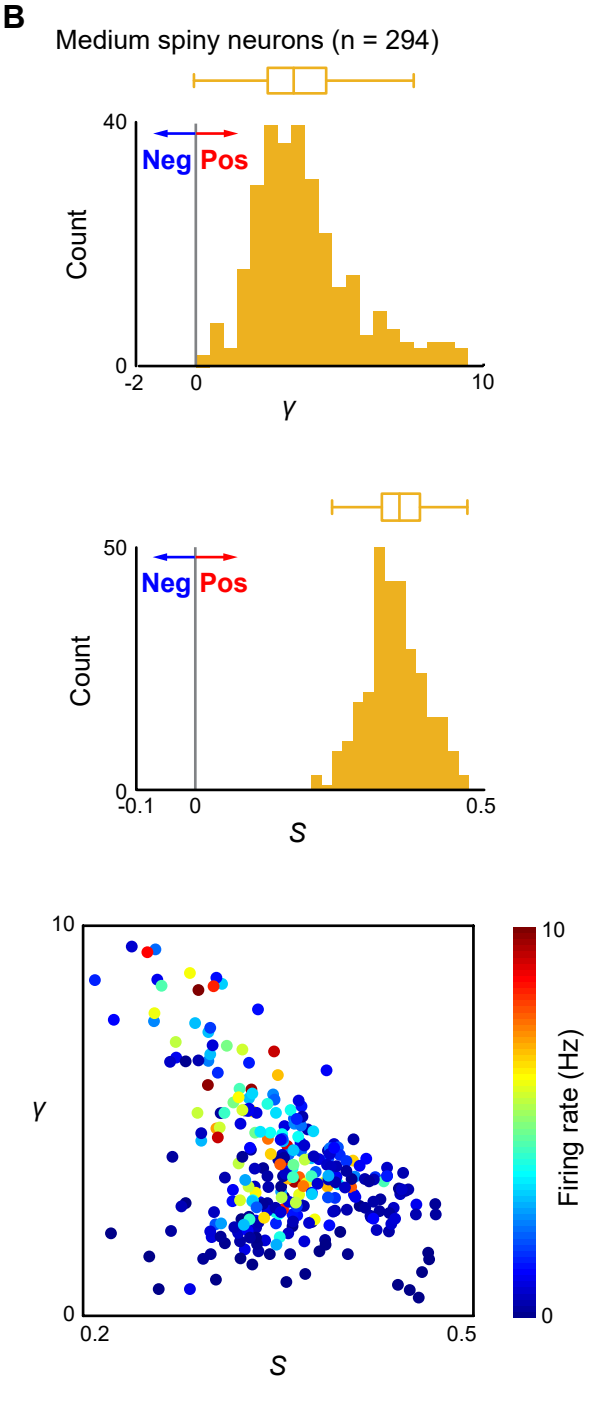
Medium spiny neurons (n = 294)
Count
40
0
Neg
Pos
-2
0
10
γ
Count
50
0
Neg
Pos
-0.1
0
0.5
S
10
γ
0
0.2
0.5
S
10
Firing rate (Hz)
0

C

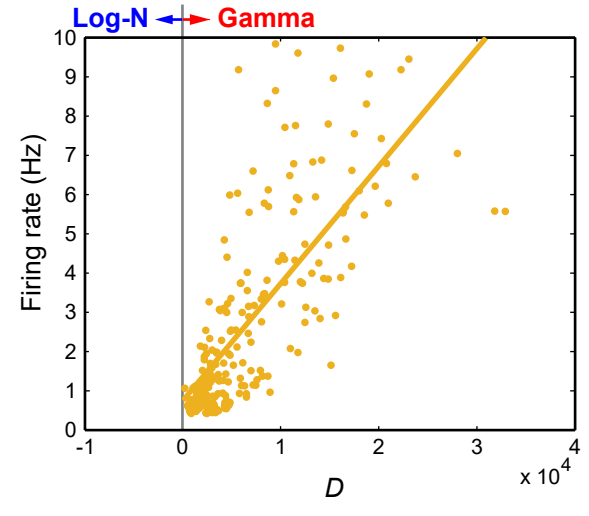
Log-N
Gamma
Firing rate (Hz)
10
9
8
7
6
5
4
3
2
1
0
-1
0
1
2
3
4
x 10^4
D

Figure 8

A

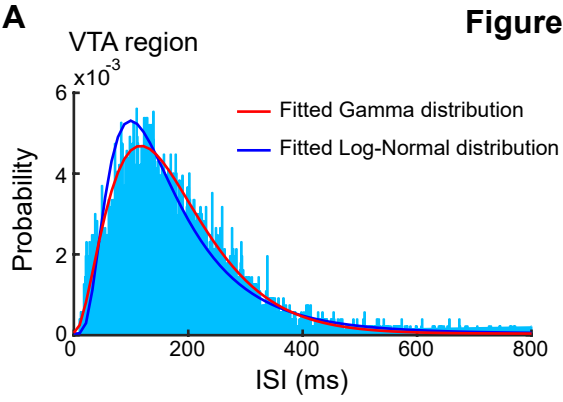
VTA region
x10^-3
Fitted Gamma distribution
Fitted Log-Normal distribution
Probability
ISI (ms)
0
2
4
6
0
200
400
600
800

B

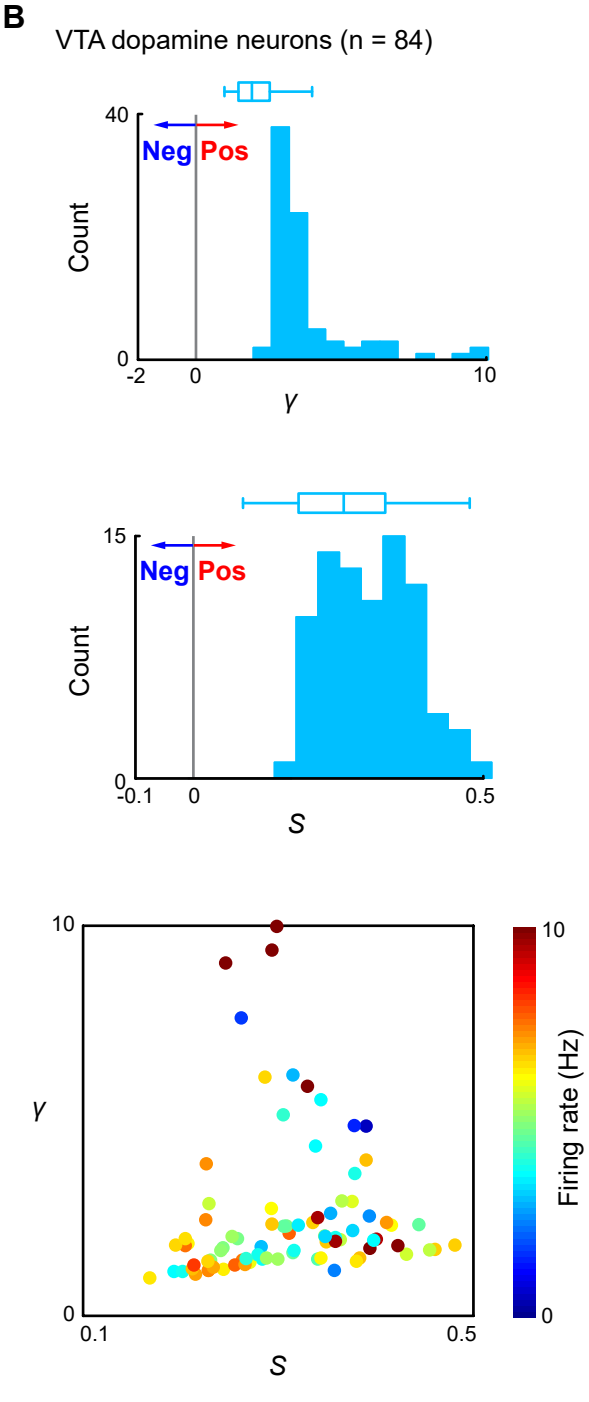
VTA dopamine neurons (n = 84)
Neg
Pos
Count
γ
40
0
-2
0
10
Neg
Pos
Count
S
15
0
-0.1
0
0.5
γ
S
10
0
0.1
0.5
Firing rate (Hz)
10
0

C

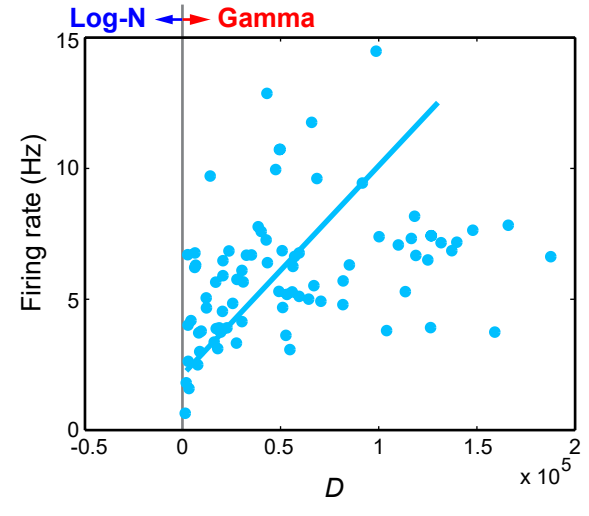
Log-N
Gamma
Firing rate (Hz)
D
x 10^5
15
10
5
0
-0.5
0
0.5
1
1.5
2

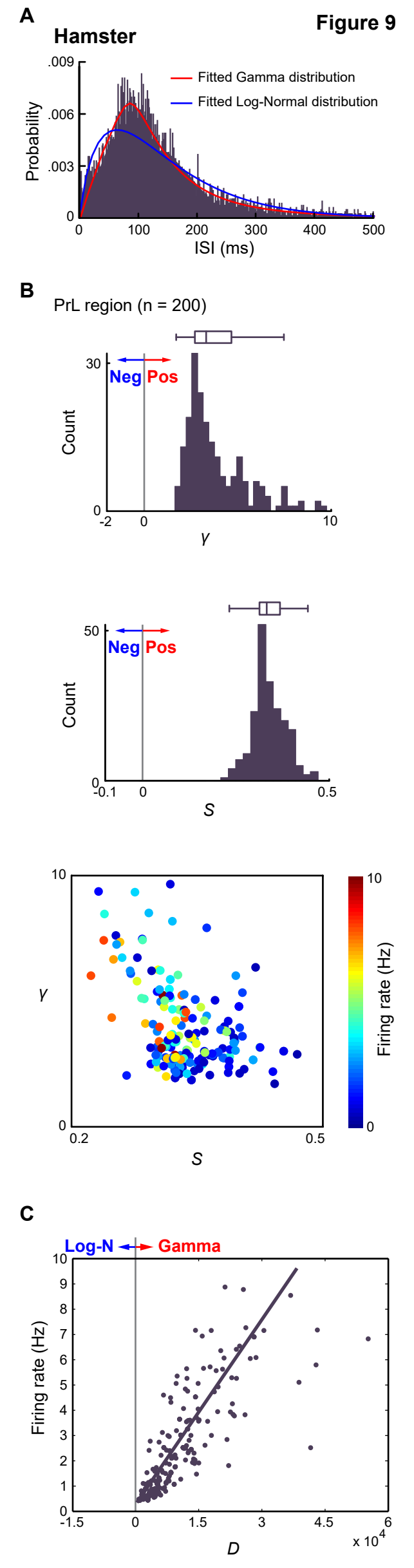
A
Hamster
Figure 9
Fitted Gamma distribution
Fitted Log-Normal distribution
Probability
.009
.006
.003
0
0
100
200
300
400
500
ISI (ms)
B
PrL region (n = 200)
Neg
Pos
Count
30
0
-2
0
10
γ
Neg
Pos
Count
50
0
-0.1
0
0.5
S
10
γ
0
0.2
0.5
S
10
Firing rate (Hz)
0
C
Log-N
Gamma
Firing rate (Hz)
10
9
8
7
6
5
4
3
2
1
0
-1.5
0
1.5
3
4.5
6
x 10^4
D

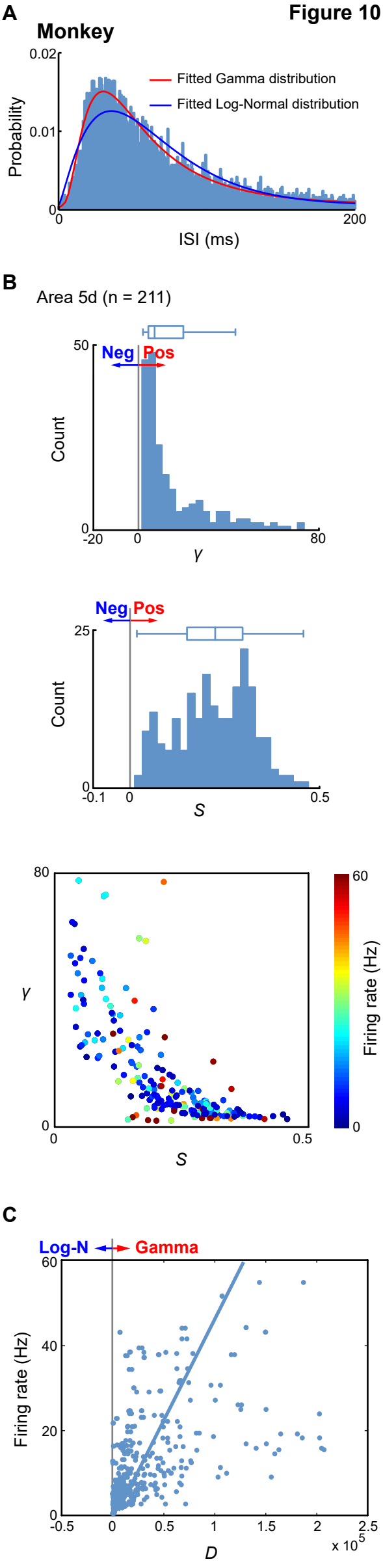

A
Figure 10
Monkey
Fitted Gamma distribution
Fitted Log-Normal distribution
Probability
0.02
0.01
0
0
200
ISI (ms)
B
Area 5d (n = 211)
Neg
Pos
Count
50
0
-20
0
80
γ
Neg
Pos
Count
25
0
-0.1
0
0.5
S
80
γ
0
0
0.5
S
60
Firing rate (Hz)
0
C
Log-N
Gamma
Firing rate (Hz)
60
40
20
0
-0.5
0
0.5
1
1.5
2
2.5
x 10^5
D

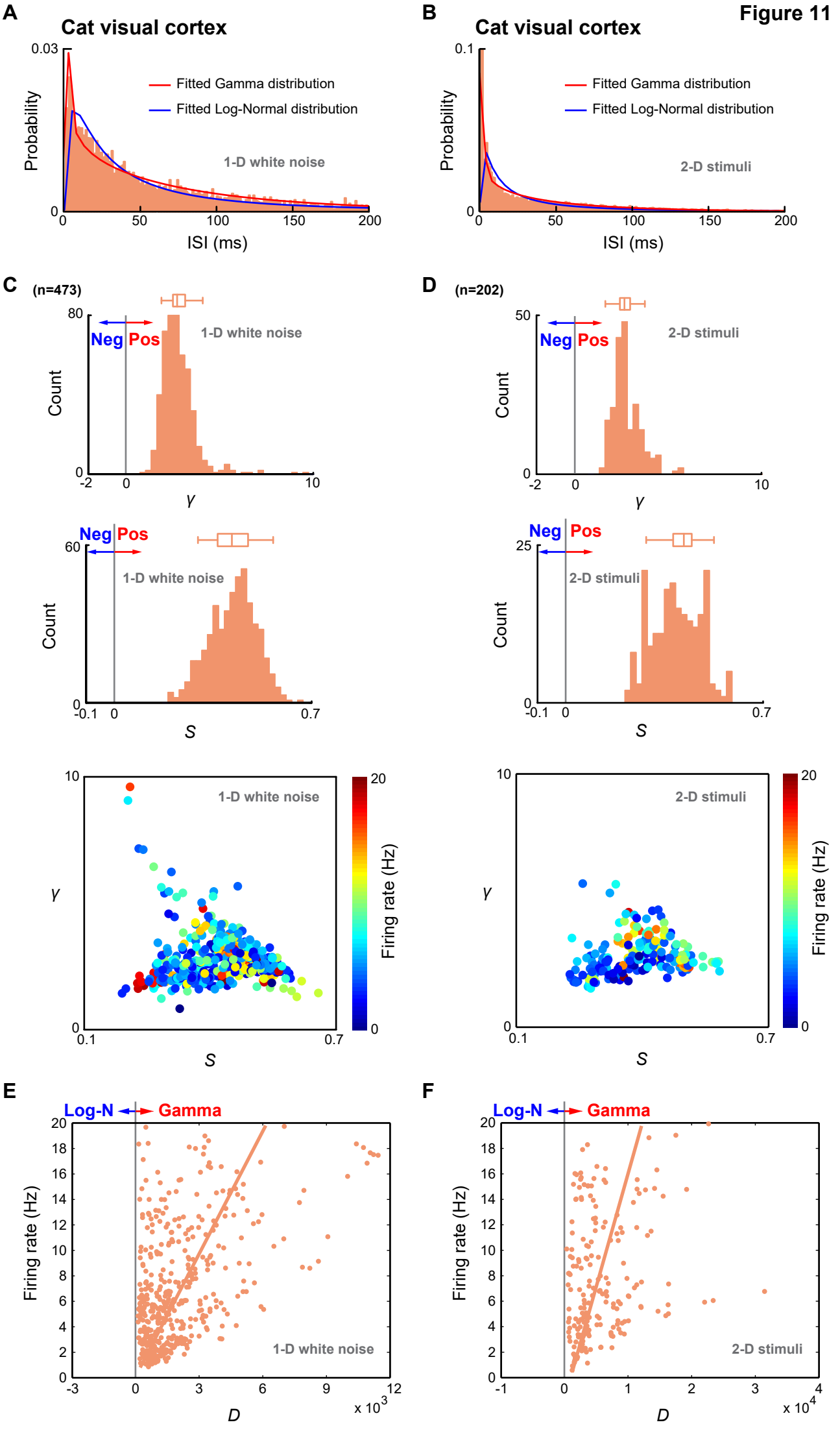
Figure 11
A
Cat visual cortex
Probability
Fitted Gamma distribution
Fitted Log-Normal distribution
1-D white noise
ISI (ms)
B
Cat visual cortex
Probability
Fitted Gamma distribution
Fitted Log-Normal distribution
2-D stimuli
ISI (ms)
C
(n=473)
Neg
Pos
1-D white noise
Count
γ
S
D
(n=202)
2-D stimuli
Firing rate (Hz)
E
Log-N
Gamma
Firing rate (Hz)
D
x 10^3
F
x 10^4

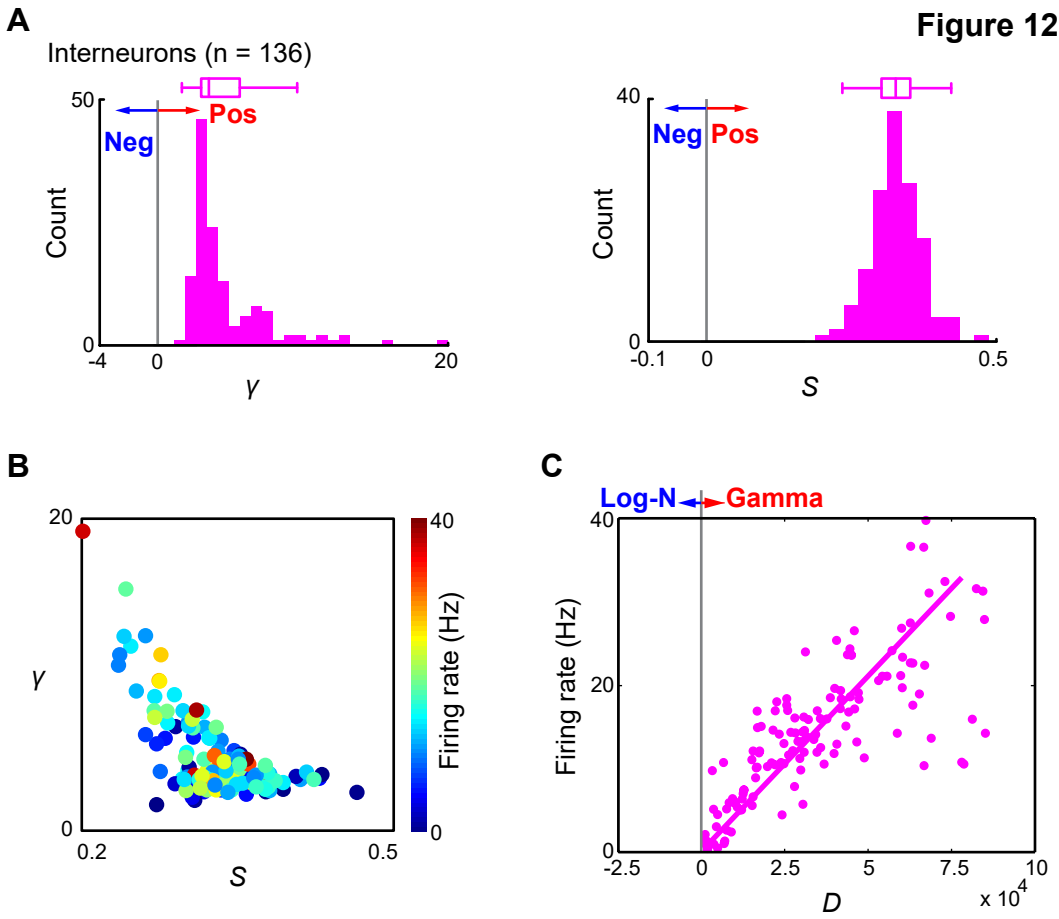

A
Figure 12
Interneurons (n = 136)
Neg
Pos
Count
50
0
-4
0
20
γ
Neg
Pos
Count
40
0
-0.1
0
0.5
S
B
20
0
0.2
0.5
γ
S
40
0
Firing rate (Hz)
C
Log-N
Gamma
Firing rate (Hz)
40
20
0
-2.5
0
2.5
5
7.5
10
x 10^4
D

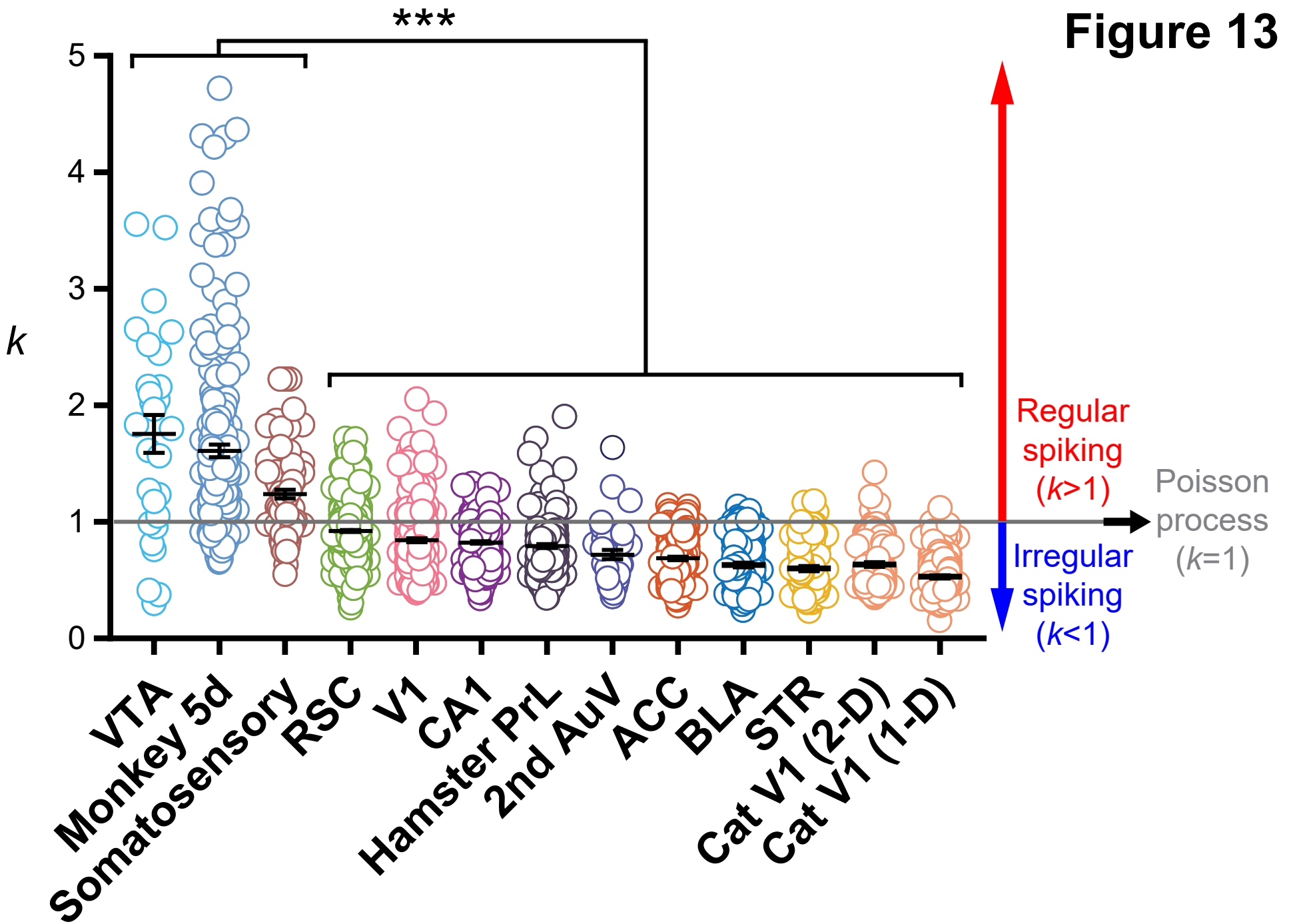
Figure 13
***
k
5
4
3
2
1
0
Regular spiking (k>1)
Poisson process (k=1)
Irregular spiking (k<1)
VTA
Monkey 5d
Somatosensory
RSC
V1
CA1
Hamster PrL
2nd AuV
ACC
BLA
STR
Cat V1 (2-D)
Cat V1 (1-D)

Figure 14

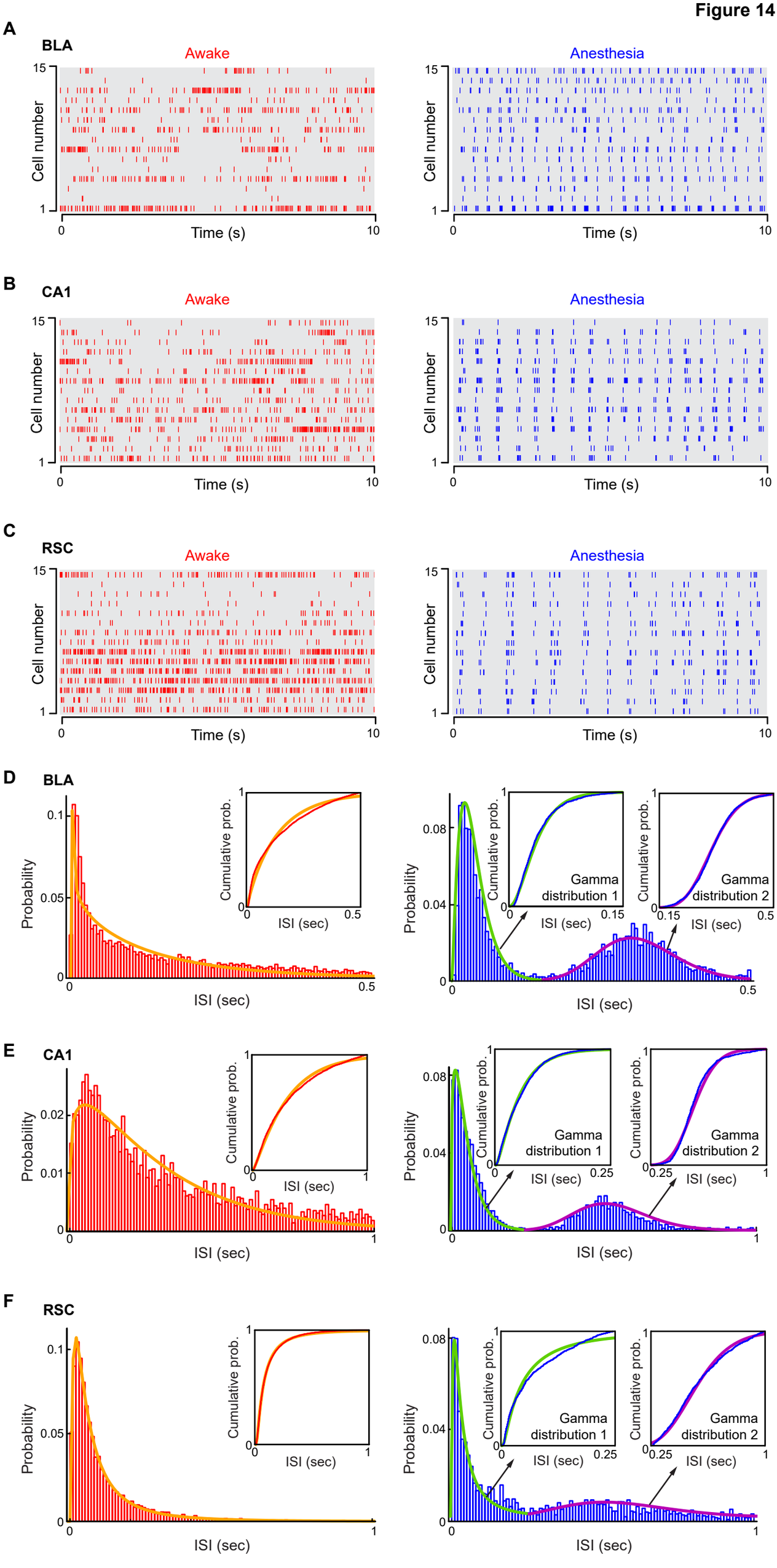
A
BLA
Awake
Anesthesia
Cell number
Time (s)
B
CA1
C
RSC
D
Probability
Cumulative prob.
ISI (sec)
Gamma distribution 1
Gamma distribution 2
E
F